

THE CHEMICAL COMPOSITION OF RED GIANT BRANCH STARS IN THE GALACTIC GLOBULAR CLUSTERS NGC 6342 AND NGC 6366

Christian I. Johnson^{1,2}, Nelson Caldwell¹, R. Michael Rich³, Catherine A. Pilachowski⁴, and Tiffany Hsyu⁵

ABSTRACT

We present radial velocities and chemical abundances for red giant branch stars in the Galactic bulge globular clusters NGC 6342 and NGC 6366. The velocities and abundances are based on measurements of high resolution ($R \gtrsim 20,000$) spectra obtained with the MMT–Hectochelle and WIYN–Hydra spectrographs. We find that NGC 6342 has a heliocentric radial velocity of $+112.5 \text{ km s}^{-1}$ ($\sigma = 8.6 \text{ km s}^{-1}$), NGC 6366 has a heliocentric radial velocity of -122.3 km s^{-1} ($\sigma = 1.5 \text{ km s}^{-1}$), and that both clusters have nearly identical metallicities ($[\text{Fe}/\text{H}] \approx -0.55$). NGC 6366 shows evidence of a moderately extended O–Na anti-correlation, but more data are needed for NGC 6342 to determine if this cluster also exhibits the typical O–Na relation likely found in all other Galactic globular clusters. The two clusters are distinguished from similar metallicity field stars as having larger $[\text{Na}/\text{Fe}]$ spreads and enhanced $[\text{La}/\text{Fe}]$ ratios, but we find that NGC 6342 and NGC 6366 display α and Fe–peak element abundance patterns that are typical of other metal-rich ($[\text{Fe}/\text{H}] > -1$) inner Galaxy clusters. However, the median $[\text{La}/\text{Fe}]$ abundance may vary from cluster–to–cluster.

Subject headings: stars: abundances, globular clusters: general, globular clusters: individual (NGC 6342, NGC 6366)

¹Harvard–Smithsonian Center for Astrophysics, 60 Garden Street, MS–15, Cambridge, MA 02138, USA; cjohnson@cfa.harvard.edu; ncaldwell@cfa.harvard.edu

²Clay Fellow

³Department of Physics and Astronomy, UCLA, 430 Portola Plaza, Box 951547, Los Angeles, CA 90095–1547, USA; rmr@astro.ucla.edu

⁴Astronomy Department, Indiana University Bloomington, Swain West 319, 727 East 3rd Street, Bloomington, IN 47405–7105, USA; cpilacho@indiana.edu

⁵UCO/Lick Observatory, University of California, 1156 High Street, Santa Cruz, CA 95064, USA; thsyu@ucsc.edu

1. INTRODUCTION

Globular cluster systems offer insights into a galaxy’s chemical evolution, star formation history, dynamical evolution, and merger history. In the Milky Way, globular clusters are often categorized based on characteristics such as chemical composition, age, horizontal branch morphology, and kinematics. The observed metallicity distribution function of Galactic globular clusters is largely bimodal with approximately 2/3 of clusters belonging to a metal–poor group that peaks near $[Fe/H]^1 \sim -1.5$ and 1/3 of clusters belonging to a metal–rich group that peaks near $[Fe/H] \sim -0.5$ (e.g., Freeman & Norris 1981; Zinn 1985; Bica et al. 2006). Furthermore, while metal–poor globular clusters are distributed across a wide range of galactocentric radii and are mostly associated with the Galactic halo, metal–rich clusters form a more flattened population that is concentrated near the inner few kpc of the Galaxy (e.g., Zinn 1985; van den Bergh 2003; Rossi et al. 2015). Recent work suggests that a majority of the inner Galaxy globular clusters with $[Fe/H] \gtrsim -1$ are members of the Galactic bulge/bar system (e.g., Minniti 1995; Côté 1999; Rossi et al. 2015). Interestingly, some age–metallicity relations find that the central metal–rich globular cluster population may even be coeval with, and in some cases older than (e.g., NGC 6522; Barbuy et al. 2009), some of the more metal–poor halo clusters (e.g., Marín–Franch et al. 2009; Forbes & Bridges 2010). In contrast, VandenBerg et al. (2013) find that clusters with $[Fe/H] > -1$ are younger than those with $[Fe/H] < -1$, and also do not find a strong correlation between galactocentric distance and age.

Although inner Galaxy globular clusters are not as extensively studied as their halo counterparts (e.g., see reviews by Kraft 1994; Gratton et al. 2004; Gratton et al. 2012), several bulge clusters are known to exhibit unusual chemical and/or morphological characteristics. For example, Haute–Provence 1 (HP–1) is located near the Galactic center and is relatively metal–rich at $[Fe/H] = -1$, but the cluster contains a prominent blue horizontal branch and no red horizontal branch stars (Ortolani et al. 1997; Barbuy et al. 2006; Ortolani et al. 2011). Similarly, the bulge clusters NGC 6388 and NGC 6441 have $[Fe/H] \sim -0.4$ (e.g., Gratton et al. 2006; Carretta et al. 2007; Gratton et al. 2007; Origlia et al. 2008), anomalous red giant branch (RGB) bumps (Nataf et al. 2013), and dominant red horizontal branches accompanied by very extended blue horizontal branches (e.g., Rich et al. 1997; Bellini et al. 2013). For HP–1, NGC 6388, and NGC 6441, the presence of a significant population of blue horizontal branch stars is not expected given the clusters’ metallicities. In a similar sense, the bulge globular clusters NGC 6440 and NGC 6569 exhibit double red clumps that are so far observed only in near infrared color–magnitude diagrams (Mauro et

¹ $[A/B] \equiv \log(N_A/N_B)_{\text{star}} - \log(N_A/N_B)_{\odot}$ and $\log \epsilon(A) \equiv \log(N_A/N_H) + 12.0$ for elements A and B.

al. 2012). The underlying cause of the double red clump feature in these clusters is not yet clear, but in Terzan 5 a double red clump has been linked to multiple stellar populations with metallicities that range from $[\text{Fe}/\text{H}] \sim -0.8$ to $+0.3$ (Ferraro et al. 2009; Origlia et al. 2011; Origlia et al. 2013). Detailed spectroscopic analyses by Origlia et al. (2011; 2013) have further revealed that the chemical composition of each population appears to match that found in bulge field stars, which supports the suggestion by Ferraro et al. (2009) that Terzan 5 may be a remnant primordial building block of the Galactic bulge.

The bulge globular clusters preserve chemical information about the early proto–bulge environment. Therefore, understanding the connection between the bulge clusters and the broader bulge/bar system is necessary for interpreting the complex chemodynamical stellar populations that currently reside in the inner Galaxy. However, only a handful of bulge clusters have been examined in detail using high resolution spectroscopy. Contamination from the bulge field star population and strong differential reddening complicate both integrated light and color–magnitude diagram analyses of bulge globular clusters. Therefore, we provide here new composition and kinematic analyses of the moderately metal–rich bulge globular clusters NGC 6342 and NGC 6366, based on high resolution optical spectra obtained with the MMT–Hectochelle and WIYN–Hydra spectrographs. Low resolution spectroscopic analyses and color–magnitude diagram fits estimate that both clusters have $[\text{Fe}/\text{H}] \sim -0.6$ (e.g., Da Costa & Seitzer 1989; Heitsch & Richtler 1999; Valenti et al. 2004; Origlia et al. 2005a; Saviane et al. 2012; Campos et al. 2013), but only NGC 6342 has had some of its stars (4; Origlia et al. 2005a) examined via high resolution spectroscopy. Although little is known about the chemical composition of NGC 6366, the cluster is particularly noteworthy because it has an unusual bottom–light mass function (Paust et al. 2009). NGC 6366 also has a very low velocity dispersion of $\sim 1 \text{ km s}^{-1}$ (Da Costa & Seitzer 1989; Rutledge et al. 1997), and may have experienced significant tidal stripping and mass loss (Paust et al. 2009).

In this paper, we examine the light odd–Z, α , Fe–peak, and heavy element abundance patterns of NGC 6342 and NGC 6366 to compare with those of similar metallicity bulge cluster and field stars. The addition of these new data to the literature will: allow for an investigation of the chemical similarities and differences between bulge cluster and field stars, define the RGB sequence of each cluster, permit further investigation into whether or not the typical light element abundance variations found in nearly all metal–poor clusters extend also to metal–rich bulge clusters, and help constrain the contribution of dissolved globular clusters to the bulge field.

2. OBSERVATIONS, TARGET SELECTION, AND DATA REDUCTION

2.1. Observations and Target Selection

The spectra for this project were obtained using the Hectochelle (Szentgyorgyi et al. 2011) and Hydra (Bershady et al. 2008; Knezeck et al. 2010) multi-fiber bench spectrographs mounted on the MMT 6.5m and WIYN 3.5m telescopes, respectively. NGC 6342 was observed with Hectochelle on 18 June 2014 and also with Hydra on 27 June 2013. However, NGC 6366 was only observed with Hydra on 18 May 2012. The Hectochelle observations consisted of a 2400 and 2065 sec exposure set using the 110 line mm^{-1} Echelle grating, the “CJ26” filter, and 2×1 (spatial \times dispersion) binning to achieve a resolving power of $R \equiv \lambda/\Delta\lambda \approx 38,000$. Similarly, the Hydra observations consisted of 3×3600 sec exposures with the bench configured to use the 316 line mm^{-1} Echelle grating, the X18 filter, the red camera and fibers, and 2×1 binning to achieve a resolving power of $R \approx 18,000$. The spectra spanned approximately 6140–6310 Å for the Hectochelle data and 6080–6390 Å for the Hydra data.

The target stars for both clusters were selected using photometry and coordinates available through the Two Micron All Sky Survey (2MASS; Skrutskie et al. 2006) database. Since both clusters are located at relatively low Galactic latitudes near the bulge, the fiducial RGB sequences for each cluster are hidden by the significant stellar crowding. Identifying the cluster RGB sequences is further complicated because the cluster stars and a large fraction of the outer bulge field stars share similar metallicities. Both clusters also are affected by significant reddening with NGC 6342 having $E(\text{B}-\text{V}) \approx 0.60$ and $\Delta E(\text{B}-\text{V}) \approx 0.40$ (Heitsch & Richtler 1999; Valenti et al. 2004; Alonso-García et al. 2012) and NGC 6366 having $E(\text{B}-\text{V}) \approx 0.70$ and $\Delta E(\text{B}-\text{V}) \approx 0.05$ (Alonso et al. 1997; Sarajedini et al. 2007; Paust et al. 2009; Dotter et al. 2010; Campos et al. 2013). The combination of these effects makes it difficult to know *a priori* which stars are true cluster members.

Therefore, we repeated the selection procedure used in Johnson et al. (2015) to identify cluster members in the bulge globular cluster NGC 6273. Briefly, we assumed the cluster RGB sequences could be reasonably well traced using only stars within $2'$ of each cluster’s core. The selection region was then broadened to include the effects of differential reddening, and stars were prioritized in the fiber assignment codes according to the distance between a star and the cluster core. A total of 216 fibers were placed on targets with Hectochelle for NGC 6342 and 51 fibers were placed on NGC 6342 targets with Hydra. Similarly, 51 Hydra fibers were also placed on targets for NGC 6366. The final selection of targets is illustrated in Figure 1 for NGC 6342 and Figure 2 for NGC 6366. The significantly larger differential reddening in NGC 6342 is clearly evident when comparing Figures 1 and 2, and is largely the cause of the significantly lower percentage of radial velocity members found in NGC

6342 (8%) versus NGC 6366 (37%; see also Section 4). The strict fiber-to-fiber distance restrictions of Hectochelle and Hydra contribute further to the low membership percentages because the magnetic buttons cannot be packed efficiently near the cluster cores, where the field contamination is at a minimum. The star identifications, J2000 coordinates, 2MASS photometry, and radial velocity measurements for all member and non-member stars are provided in Tables 1–2.

2.2. Data Reduction

The data reduction process for both the Hectochelle and Hydra spectra was carried out using standard IRAF² tasks. The raw spectra were bias subtracted and trimmed before the more specialized tasks of aperture identification and tracing, scattered light removal, flat-field correction, ThAr wavelength calibration, cosmic-ray removal, spectrum extraction, and sky subtraction were carried out. Note that the sky subtraction was performed using simultaneous sky spectra obtained with fibers placed on “blank” sky regions in the Hectochelle and Hydra fields-of-view. While a majority of the Hydra data reduction was performed using the IRAF task *dohydra*, most of the Hectochelle reduction procedures were carried out by a dedicated pipeline maintained at the Smithsonian Astrophysical Observatory’s Telescope Data Center.

The final data reduction steps of telluric subtraction, continuum fitting, and spectrum combining were carried out using the IRAF tasks *telluric*, *continuum*, and *scombine* outside the general pipelines. The final combined spectra yielded signal-to-noise (S/N) ratios of approximately 50–100 per resolution element. Due to higher extinction, worse observing conditions, and shorter exposures (for Hectochelle), the NGC 6342 data tended to have lower S/N than the NGC 6366 data. However, we only measured abundances in stars with the highest quality spectra, and for which we could measure >10 Fe I lines (see Table 3).

²IRAF is distributed by the National Optical Astronomy Observatory, which is operated by the Association of Universities for Research in Astronomy, Inc., under cooperative agreement with the National Science Foundation.

3. DATA ANALYSIS

3.1. Model Atmospheres

The model atmosphere parameters effective temperature (T_{eff}), metallicity ([M/H]), and microturbulence ($\xi_{\text{mic.}}$) were determined using spectroscopic methods. Specifically, temperatures were set by removing any trends in plots of $\log \epsilon(\text{Fe I})$ abundance versus excitation potential, and microturbulence values were set by removing any trends in plots of $\log \epsilon(\text{Fe I})$ abundance versus reduced equivalent width³ (EW). The model atmosphere metallicities were set to the measured [Fe/H] values.

In Figure 3, we compare the spectroscopic T_{eff} values derived using excitation equilibrium with the $J-K_S$ color–temperature relation provided by González Hernández & Bonifacio (2009), assuming $E(B-V) = 0.57$ for NGC 6342 (Valenti et al. 2004) and $E(B-V) = 0.70$ for NGC 6366 (Alonso et al. 1997). Despite the presence of significant differential reddening in both clusters, the two temperature scales are well-correlated. We find an average offset (ΔT_{eff}), in the sense of photometric T_{eff} minus spectroscopic T_{eff} , to be $\Delta T_{\text{eff}} = -32$ K ($\sigma = 138$ K) for NGC 6342 and $\Delta T_{\text{eff}} = +77$ K ($\sigma = 131$ K) for NGC 6366. Although the agreement is comparable to the 94 K standard deviation of the color–temperature relation (see González Hernández & Bonifacio 2009; their Table 5), the removal of one significant outlier in NGC 6342 and two significant outliers in NGC 6366 decreases the offsets to $\Delta T_{\text{eff}} = +32$ K ($\sigma = 77$ K) and $\Delta T_{\text{eff}} = +33$ K ($\sigma = 83$ K), respectively.

Since the data span a limited wavelength range, we did not constrain surface gravities ($\log(g)$) by setting ionization equilibrium between neutral and singly ionized species (e.g., Fe I/II). Instead, we estimated surface gravities using isochrones available through the Dartmouth Stellar Evolution database (Dotter et al. 2008). We used the online interpolator⁴ to obtain a surface gravity value for each star, given its spectroscopically determined temperature. We assumed a standard helium mass fraction, $[\alpha/\text{Fe}] = +0.4$ (Origlia et al. 2005a; see also Section 5), and an age of 11 Gyr for both clusters (e.g., Campos et al. 2013; VandenBerg et al. 2013).

Each model atmosphere was calculated by interpolating within the α -enhanced ATLAS9 grid (Castelli & Kurucz 2004)⁵. The final values were determined by simultaneously

³The reduced equivalent width is defined as $\log(\text{EW}/\lambda)$.

⁴The Dartmouth Stellar Evolution database online interpolator can be accessed at: http://stellar.dartmouth.edu/models/isolf_new.html.

⁵The model atmosphere grid can be accessed at: <http://wwwuser.oats.inaf.it/castelli/grids.html>.

solving for temperature, metallicity, and microturbulence and iteratively redetermining surface gravity via the isochrone interpolator mentioned above. The final adopted parameters for NGC 6342 (4 stars) and NGC 6366 (13 stars) are provided in Table 3.

3.2. Abundance Analysis

The abundance analysis for this work closely follows that described in Johnson et al. (2014). Briefly, the abundances of Si, Ca, Cr, Fe, and Ni were calculated using the *abfind* driver of the LTE line analysis code MOOG (Sneden 1973; 2014 version). Similarly, the abundances of O, Na, Mg, and La were determined using the *synth* driver of MOOG to minimize differences between the observed and synthetic spectra. All EWs were measured using the semi-automated code outlined in Johnson et al. (2014) that fits single or multiple Gaussian profiles to isolated and blended absorption lines.

Since previous estimates indicate that both clusters should have $[\text{Fe}/\text{H}] \sim -0.6$ (see Section 1), we performed a differential abundance analysis relative to the giant star Arcturus ($[\text{Fe}/\text{H}] \approx -0.5$; e.g., Ramírez & Allende Prieto 2011). The line list provided in Table 4 uses the same $\log(\text{gf})$ values, solar reference abundances, and Arcturus reference abundances as those in Johnson et al. (2014), but we added a few additional Fe I lines due to differences in wavelength coverage between the FLAMES, Hectochelle, and Hydra data. The only other exception to the Johnson et al. (2014) line list was our inclusion of the La atomic data from Lawler et al. (2001), which takes into account hyperfine structure introduced by the ^{139}La isotope.

For the abundances determined by spectrum synthesis, we included atomic lines from the Kurucz database⁶ and CN molecular lines from Sneden et al. (2014). The original $\log(\text{gf})$ values were manually adjusted until the synthetic spectrum matched the observed spectrum of the Arcturus atlas (Hinkle et al. 2000). We adopted the model atmosphere parameters and Arcturus abundances listed in Table 4 and Ramírez & Allende Prieto (2011) for C, N, O, Na, Mg, and La. In order to account for contributions from CN lines, we initially assumed the stars were well-mixed with $[\text{C}/\text{Fe}] = -0.30$, $[\text{N}/\text{Fe}] = +0.50$, and $^{12}\text{C}/^{13}\text{C} = 4$, which are typical values for evolved RGB stars in the bulge field and clusters (e.g., Origlia et al. 2005a; Meléndez et al. 2008; Ryde et al. 2010). Since C, N, and O are integral parts of the molecular equilibrium calculations, we first fit the 6300 [O I] line and nearby CN features to define the oxygen and C+N abundances for each star. The nitrogen abundance was treated as a free parameter in order to fit the CN line profiles. For the two stars in NGC 6342

⁶The most up-to-date line lists can be accessed at: <http://kurucz.harvard.edu/linelists/gfnew/>.

that we were not able to measure [O/Fe], we assumed [O/Fe] = +0.60, the average oxygen abundance for the other two NGC 6342 stars in our sample, and set [C/Fe] = −0.30 and [N/Fe] = +0.50.

While the 6154/6160 Å Na I and 6262 Å La II lines are relatively uncontaminated, the 6318–6319 Å Mg I triplet lines are moderately affected by a broad Ca I auto-ionization feature. In order to correct for this effect, we adjusted the log $\epsilon(\text{Ca})$ abundance until the shape of the synthetic and observed spectra matched in the nearby continuum windows (e.g., see Figure 6 of Johnson et al. 2014). The log $\epsilon(\text{Ca})$ abundance that best reproduced the auto-ionization feature tended to be \sim 0.3–0.4 dex less than the average log $\epsilon(\text{Ca})$ abundance measured from the individual atomic lines.

3.2.1. Internal Abundance Uncertainties

The largest sources of internal abundance uncertainties are typically related to the derivation of the stellar model atmosphere parameters. Additional sources, such as line blending, continuum placement, atomic parameters, and visual profile fitting, tend to have only a small effect on the final abundances derived from moderately high S/N and resolution spectra. The line profile fitting code used for this project takes into account a spectrum’s S/N and estimates the uncertainty range in continuum placement. The continuum uncertainty is then propagated through the profile fitting procedure, and the code generates an EW error estimate for every line. The average EW uncertainty ranges from approximately 10% for a line of 20 mÅ to 2% for a line of 150 mÅ. These uncertainties translate into abundance errors of \sim 0.02–0.05 dex, which are comparable to the typical standard errors of the mean derived in our analysis (\sim 0.03 dex on average). Therefore, our final internal uncertainty calculations provided in Table 5 include the error of the mean for each element as a tracer of the random measurement error.

In order to examine the internal sensitivity of the derived log $\epsilon(\text{X})$ abundances to changes in the model atmosphere parameters, we calculated the abundance differences between the “best-fit” model and those with each parameter adjusted within its estimated uncertainty range. A temperature uncertainty of 75 K was adopted based on a comparison of the spectroscopic and photometric T_{eff} values shown in Figure 3, where the 1σ star-to-star deviation, after removing three extreme outliers, is 79 K. Since the surface gravity values were determined from the isochrones described in Section 3.1, we estimated that the interpolation uncertainty for $\log(g)$ was 0.10 cgs, assuming $\Delta T_{\text{eff}} = 75$ K and $\Delta \text{age} = 1$ Gyr. The overall metallicity uncertainty was estimated to be 0.10 dex based on the star-to-star dispersion in our derived [Fe/H] values for both clusters. Finally, we estimated that the microturbulence

velocity uncertainty was 0.10 km s^{-1} , based on an examination of the line-to-line scatter in plots of $\log \epsilon(\text{Fe I})$ abundance versus reduced EW. The final abundance uncertainties, including the measurement errors described above, were added in quadrature to produce the final uncertainty values listed in Table 5. Note that the [X/Fe] ratios take into account both the errors in [Fe/H] and [X/H] for each element. The typical errors range from $\sim 0.05\text{--}0.10$ dex.

4. RADIAL VELOCITY MEASUREMENTS AND CLUSTER MEMBERSHIP

The radial velocities for both NGC 6342 and NGC 6366 were measured using the IRAF task *fxcor*, which cross correlated the observed spectra with a convolved and rebinned version of the Arcturus atlas (Hinkle et al. 2000) that matches the resolution and sampling of the Hectochelle and Hydra spectra. We avoided contamination due to any residual telluric lines by only using the 6120–6275 Å region for the cross correlation. The heliocentric corrections were determined using the information in the image headers and the IRAF task *rvcor*. Since there were two exposures for the Hectochelle data and three exposures each for the Hydra data, we measured the heliocentric radial velocity ($\text{RV}_{\text{helio.}}$) in each exposure and treated these values as independent measurements. The standard deviation of these measurements for each star are listed in Tables 1–2 as the $\text{RV}_{\text{helio.}}$ errors. The average $\text{RV}_{\text{helio.}}$ error for the entire sample is 0.38 km s^{-1} ($\sigma = 0.31 \text{ km s}^{-1}$); however, the Hectochelle data have a higher resolution and thus a lower average error of 0.35 km s^{-1} ($\sigma = 0.20 \text{ km s}^{-1}$) compared to the 0.44 km s^{-1} ($\sigma = 0.45 \text{ km s}^{-1}$) average error for the Hydra data.

Three stars in the field of NGC 6342 (2MASS 17221115–1931581, 17213359–1940422, and 17212139–1934169) were observed with both Hectochelle and Hydra (see also Table 1), and the independent $\text{RV}_{\text{helio.}}$ measurements permit a rough estimate of the zero point offset between the two observing runs. The $\text{RV}_{\text{helio.}}$ differences, in the sense of Hectochelle minus Hydra, are $+0.18 \text{ km s}^{-1}$, $+6.10 \text{ km s}^{-1}$, and $+1.11 \text{ km s}^{-1}$ for 2MASS 17221115–1931581, 17213359–1940422, and 17212139–1934169, respectively. If we neglect the large $\text{RV}_{\text{helio.}}$ difference for 2MASS 17213359–1940422, which could be a velocity variable or binary star, the average zero point offset between Hectochelle and Hydra is $+0.65 \text{ km s}^{-1}$.

Given the significant stellar crowding, differential reddening, and similar metallicities of bulge field stars to the NGC 6342 and NGC 6366 cluster stars, radial velocities are useful indicators of cluster membership. Previous analyses measured heliocentric radial velocities of NGC 6342 that range from $\sim +114$ to $+118 \text{ km s}^{-1}$ with velocity dispersions that range from $\sim 5\text{--}8 \text{ km s}^{-1}$ (Dubath et al. 1997; Origlia et al. 2005; Caselli–Dinescu et al. 2010).

Similarly, the heliocentric radial velocity estimates for NGC 6366 range from -122.6 to -123.2 km s $^{-1}$, but the dispersion is estimated to be only ~ 1 km s $^{-1}$ (Da Costa & Seitzer 1989; Rutledge et al. 1997). We find in agreement with past work that the average RV_{helio} of NGC 6342 is $+112.5$ km s $^{-1}$ ($\sigma = 8.6$ km s $^{-1}$) and that of NGC 6366 is -122.3 km s $^{-1}$ ($\sigma = 1.5$ km s $^{-1}$).

Although the broad radial velocity distribution of the bulge field stars is consistent with observations from recent large sample studies (e.g., Kunder et al. 2012; Ness et al. 2013; Zoccali et al. 2014), the field contamination makes assigning membership more difficult in the NGC 6342 field than the NGC 6366 field (see Figure 4). Therefore, we have only included stars with RV_{helio} values between 95 – 130 km s $^{-1}$ ($\sim 2\sigma$) as possible cluster members for NGC 6342. Nevertheless, as mentioned in Section 2.1, only 8% and 37% of the observed targets are likely radial velocity members of NGC 6342 and NGC 6366, respectively. However, a high contamination rate of field stars is typical for bulge globular cluster observations that extend far beyond the cluster core (e.g., Gratton et al. 2007).

5. RESULTS AND DISCUSSION

5.1. Comparing NGC 6342 and NGC 6366

As mentioned in Section 1, neither NGC 6342 nor NGC 6366 has been extensively studied with high resolution spectroscopy. Origlia et al. (2005a) obtained high resolution infrared spectra of four RGB stars in NGC 6342 and found the cluster to be only moderately metal-poor ($\langle [Fe/H] \rangle = -0.60$), enhanced in all α -elements ($\langle [\alpha/Fe] \rangle = +0.34$), and exhibit a small star-to-star dispersion in [O/Fe] ($\Delta[O/Fe] = 0.04$ dex). NGC 6366 has never been analyzed with high resolution spectroscopy, but photometric analyses suggest that the cluster may host at least two populations with different light element chemistry (Piotto et al. 2015; their Figure 14). Photometric and low/moderate resolution spectroscopy further indicate that NGC 6366 is comparable in metallicity to NGC 6342, with estimates ranging from $[Fe/H] = -0.85$ to -0.54 (Johnson et al. 1982; Da Costa & Seitzer 1989; Da Costa & Armandroff 1995; Alonso et al. 1997; Dotter et al. 2010; Saviane et al. 2012; Campos et al. 2013).

The chemical composition results presented here, including 4 RGB stars for NGC 6342 and 13 RGB stars for NGC 6366, are in general agreement with previous work. For NGC 6342, we find an average $[Fe/H] = -0.53$ ($\sigma = 0.11$), significantly enhanced [O/Fe] ($\langle [O/Fe] \rangle = +0.61$) with smaller enhancements for the heavier α -elements ($\langle [\alpha/Fe] \rangle = +0.33$), and a moderate spread in [O/Fe] ($\Delta[O/Fe] = 0.32$). For NGC 6366, we find an average $[Fe/H]$

$= -0.55$ ($\sigma = 0.09$), a slightly lower average $[\text{O}/\text{Fe}] = +0.51$ with similar enhancements for the heavier α -elements ($\langle [\alpha/\text{Fe}] \rangle = +0.29$), and a slightly larger spread in $[\text{O}/\text{Fe}]$ ($\Delta[\text{O}/\text{Fe}] = 0.40$). Both clusters also exhibit moderate enhancements and dispersions of $[\text{Na}/\text{Fe}]$, and possibly $[\text{La}/\text{Fe}]$, but the Fe-peak elements in both clusters mostly track iron⁷. The data indicate that NGC 6366 may have $[\text{Cr}/\text{Fe}]$ and $[\text{Ni}/\text{Fe}]$ abundances that are ~ 0.1 dex higher than those of NGC 6342, but a larger sample of Fe-peak element measurements in these two clusters is needed in order to verify that this difference is real. We note that NGC 6342 and NGC 6366 have similar differences between their maximum and minimum $[\text{La}/\text{Fe}]$ abundances ($\Delta[\text{La}/\text{Fe}] \sim 0.35$ dex), but different dispersions. Therefore, the larger dispersion in NGC 6342 may be a result of the small sample size (4 stars); however, we cannot rule out that the smaller $[\text{La}/\text{Fe}]$ dispersion in NGC 6366 is a residual effect from enhanced tidal disruption (Paust et al. 2009). A summary of the average and dispersion values for every element in each star per cluster is provided in Table 6.

5.2. NGC 6342, NGC 6366, and the Bulge Globular Cluster System

In Figure 5, we compare the light element abundance patterns of individual stars in NGC 6342 and NGC 6366 with those of similar metallicity ($-0.7 \lesssim [\text{Fe}/\text{H}] \lesssim -0.4$) bulge globular clusters. The relationships between the element ratio pairs shown in Figure 5 are often interpreted as being a result of high temperature ($T \gtrsim 65 \times 10^6$ K) proton-capture burning (e.g., Langer et al. 1993; Arnould et al. 1999; Prantzos et al. 2007; Ventura et al. 2012), and as a consequence many globular clusters exhibit O-Na and Mg-Si anti-correlations concurrent with O-Mg correlations (e.g., Yong et al. 2005; Carretta et al. 2009b; Johnson & Pilachowski 2010; Cohen & Kirby 2012; Carretta et al. 2014; Yong et al. 2014; Carretta 2015; Roederer & Thompson 2015). However, as can be seen in Figure 5, NGC 6366 only shows evidence supporting the existence of a moderately extended O-Na anti-correlation. Although the NGC 6342 data overlap with the O-Na trend observed in NGC 6366 and other similar metallicity bulge clusters, we were only able to measure $[\text{O}/\text{Fe}]$ and $[\text{Na}/\text{Fe}]$ in two stars for NGC 6342 and therefore cannot comment further on the extent, or existence, of a true O-Na anti-correlation in this cluster.

The NGC 6366 data do not show significant star-to-star abundance variations or correlations for $[\text{Mg}/\text{Fe}]$ and $[\text{Si}/\text{Fe}]$, and from these data we can speculate that the gas from which the cluster stars formed did not reach temperatures hot enough to burn significant

⁷The 0.14 dex dispersion in $[\text{Cr}/\text{Fe}]$ for NGC 6366 is likely due to increased measurement errors and the availability of only one weak line

amounts of Mg into Al nor Al into Si. Previous observations of metal-rich ($[Fe/H] \gtrsim -1$) globular clusters have noted similar trends of small $[Mg/Fe]$, $[Al/Fe]$, and/or $[Si/Fe]$ star-to-star abundance dispersions, and several authors have suggested that the MgAl cycle may be less efficient at higher metallicities (e.g., Carretta et al. 2004; Carretta et al. 2007; Carretta et al. 2009b; O’Connell et al. 2011; Cordero et al. 2014, 2015). Although larger samples are still needed, the observations of NGC 6342 and NGC 6366 provided here support this idea. The current work and literature data shown in Figure 5 suggest that most globular clusters with $-0.7 \lesssim [Fe/H] \lesssim -0.4$ have about the same $[Mg/Fe]$ and $[Si/Fe]$ distributions, regardless of the extent of their O–Na anti-correlations.

In Figure 6, we plot the median $[X/Fe]$ ratios and dispersions as a function of $[Fe/H]$ for NGC 6342, NGC 6366, and several other metal-rich ($[Fe/H] \gtrsim -1$) bulge globular clusters available in the literature. We find that the median $[X/Fe]$ ratios and dispersions of most elements in NGC 6342 and NGC 6366 are in good agreement with other similar metallicity globular clusters (see also Table 6). Although the similar abundance trends of most elements heavier than Na in Figure 6 suggest a common formation environment, the different $[La/Fe]$ distributions may indicate a more heterogeneous formation process.

For example, NGC 6342, NGC 6366, and NGC 6388 (Carretta et al. 2007) all exhibit similarly enhanced $[La/Fe]$ ratios; however, HP-1 (Barbuy et al. 2006) and NGC 6553 (Alves-Brito et al. 2006) have $[La/Fe] \lesssim 0$. Barbuy et al. (2009) noted a similar trend that stars in NGC 6522 were significantly more Ba/La-enhanced than those of HP-1 and NGC 6558, despite all three clusters sharing roughly similar $[Fe/H]$, α -element, and O–Na distributions. Additionally, Gratton et al. (2006) found that bulge clusters largely exhibited similar abundance patterns, but that certain elements, such as Mn, may vary from cluster-to-cluster. Therefore, unlike the α -elements Mg, Si, and Ca, which appear similarly enhanced for nearly all metal-rich bulge clusters, the heavy elements may provide some discrimination regarding how, or where, inner Galaxy clusters formed. The current data are insufficient to provide any definitive links between bulge clusters with similar heavy element abundances, but increased sample sizes will aid in the interpretation of the observed cluster-to-cluster heavy element abundance variations.

5.3. Comparing Bulge Globular Clusters and Field Stars

For stars with $[Fe/H] \lesssim -0.4$, previous investigations have largely found that the bulge globular cluster and field star populations share similar compositions (e.g., Carretta et al. 2001; Gratton et al. 2006; Gonzalez et al. 2011; Origlia et al. 2011; Johnson et al. 2014). Figure 6 and Table 6 indicate that NGC 6342 and NGC 6366 continue this trend, and that

the clusters only show significantly different patterns for [Na/Fe] (larger dispersion) and [La/Fe] (higher abundances). The [O/Fe] dispersion may also be larger for some clusters compared to the field stars; however, the larger measurement errors of [O/Fe], especially for field stars with uncertain gravities, make it more difficult to disentangle real scatter from measurement errors.

The larger [Na/Fe] dispersions in NGC 6342, NGC 6366, and other metal-rich bulge clusters (e.g., Gratton et al. 2007; Carretta et al. 2007; Johnson et al. 2014), compared to similar metallicity bulge field stars, are not surprising and likely a result of self-enrichment processes occurring in the cluster environments. On the other hand, the enhanced [La/Fe] abundances found in NGC 6342, NGC 6366, and NGC 6388 (Carretta et al. 2007; Worley & Cottrell 2010) stars may be a reflection of the broader Galactic globular cluster trend. In general, globular clusters tend to exhibit [Ba/Fe] and [La/Fe] ratios⁸ that increase between $[\text{Fe}/\text{H}] = -2.5$ and -1.5 , and then remain enhanced at $[\text{Ba}, \text{La}/\text{Fe}] \sim +0.3$ to at least $[\text{Fe}/\text{H}] = -0.5$ (e.g., James et al. 2004; D’Orazi et al. 2010). In contrast, bulge field stars show similar enhancements at $[\text{Fe}/\text{H}] \lesssim -1$, but the [Ba/Fe] and [La/Fe] ratios begin to decline at higher metallicity (e.g., McWilliam et al. 2010; Bensby et al. 2011; Johnson et al. 2011; Bensby et al. 2013; see also Figure 6). Therefore, the $[\text{Fe}/\text{H}] \sim -0.5$ clusters NGC 6342, NGC 6366, and NGC 6388 exhibit [La/Fe] abundances that are more similar to those of bulge field stars with $[\text{Fe}/\text{H}] \lesssim -1$. However, the different behavior of [Ba/Fe] and [La/Fe] between field and cluster stars of similar metallicity, at least between $[\text{Fe}/\text{H}] = -1$ and -0.4 , suggests that the two populations experienced different formation and s-process enrichment histories.

For metallicities higher than $[\text{Fe}/\text{H}] \sim -0.4$, some composition differences between bulge field and cluster stars may become more prevalent. In particular, Figure 6 indicates that [Mg/Fe], [Si/Fe], and [Ca/Fe] may remain enhanced to a higher metallicity in cluster stars than bulge field stars (e.g., see also Carretta et al. 2007). Since the $[\alpha/\text{Fe}]$ ratios of most clusters remain approximately constant and enhanced, at least up to $[\text{Fe}/\text{H}] \sim -0.1$, the data suggest a stronger contribution from core-collapse supernovae (e.g., Tinsley 1979), and possibly also a more rapid formation timescale, for the inner Galaxy cluster population. However, more globular cluster α -element abundance measurements, especially for clusters with $[\text{Fe}/\text{H}] \gtrsim -0.3$, are needed to definitively confirm that the most metal-rich globular clusters have higher $[\alpha/\text{Fe}]$ ratios than similar metallicity bulge field stars.

Among the heavier elements discussed here (Cr, Ni, and La), only the [La/Fe] ratios

⁸Although Ba and La isotopes can be produced in both the r-process and s-process, at $[\text{Fe}/\text{H}] \gtrsim -1$, and also in the Solar System, these elements are predominantly produced by the s-process (e.g. see reviews by Busso et al. 1999; Sneden et al. 2008).

show any evidence of discriminating bulge cluster stars from field stars at $[Fe/H] > -0.4$. The data from NGC 6553 (Alves-Brito et al. 2006) shown in Figure 6 indicate marginally higher $[La/Fe]$ abundances than the similar metallicity field stars. Similarly, Carretta et al. (2001) found the near solar metallicity bulge cluster NGC 6528 to have an average $[Ba/Fe] = +0.14$, which is again marginally higher than the roughly solar $[Ba/Fe]$ abundances found in microlensed bulge dwarf stars (Bensby et al. 2011; Bensby et al. 2013)⁹. Although more data comparing the heavy element abundance trends of metal-rich bulge cluster and field stars are needed, the small samples available so far indicate that the stronger s-process signature found in clusters near $[Fe/H] = -0.5$ may continue to at least solar metallicity.

Finally, a comparison between the chemical composition of bulge clusters with $-1 \lesssim [Fe/H] \lesssim 0$ and similar metallicity field stars suggests that the former population likely did not contribute a significant number of stars to the latter population. Second generation stars from clusters such as NGC 6388 and NGC 6441 are strongly ruled out by their very low $[O/Fe]$ and high $[Na/Fe]$ ratios, and the clusters’ first generation stars are incompatible with the field star composition based on their $[La/Fe]$ abundances. More typical clusters such as NGC 6342 and NGC 6366 are ruled out mostly by their large $[Na/Fe]$ spreads and enhanced $[La/Fe]$ abundances. Similarly, clusters with $[Fe/H] \gtrsim -0.4$ are mostly ruled out by their higher $[\alpha/Fe]$ abundances compared to the field stars. Clusters such as Terzan 5 could have contributed stars to the bulge field (e.g., see Origlia et al. 2011; Origlia et al. 2013), but it is not clear how many such objects exist nor is it clear that Terzan 5’s composition will remain compatible with the field once its $[Na/Fe]$ and heavy element abundances are measured.

6. SUMMARY

For this project, we used the MMT–Hectochelle and WIYN–Hydra spectrographs to obtain high resolution spectra of 267 RGB stars and 51 RGB stars in the bulge globular clusters NGC 6342 and NGC 6366, respectively. Cluster membership was determined primarily through radial velocity measurements. However, the significant reddening and stellar crowding along each cluster’s line-of-sight reduced the member-to-target ratio to 8% for NGC 6342 and 37% for NGC 6366. The cluster members provided average radial velocities of $+112.5 \text{ km s}^{-1}$ ($\sigma = 8.6 \text{ km s}^{-1}$) and -122.3 km s^{-1} ($\sigma = 1.5 \text{ km s}^{-1}$) for NGC 6342 and NGC 6366, respectively.

⁹The reader should note that if the Carretta et al. (2001) data are compared with the Baade’s window $[Ba/Fe]$ abundances from McWilliam & Rich (1994), both populations exhibit similar $[Ba/Fe]$ enhancements.

From the sub-sample of confirmed cluster members, we were able to measure chemical abundances of O, Na, Mg, Si, Ca, Cr, Fe, Ni, and La for four stars in NGC 6342 and 13 stars in NGC 6366 via equivalent width measurements and spectrum synthesis fitting. We find both clusters to have nearly identical metallicities with NGC 6342 having $\langle [\text{Fe}/\text{H}] \rangle = -0.53$ ($\sigma = 0.11$) and NGC 6366 having $\langle [\text{Fe}/\text{H}] \rangle = -0.55$ ($\sigma = 0.09$). Neither cluster shows significant evidence favoring a metallicity spread. Both clusters exhibit very similar average [X/Fe] ratios and star-to-star abundance variations, but O and Na are likely the only two elements that exhibit significant star-to-star scatter. NGC 6366 shows evidence of only a moderately extended O–Na anti-correlation, but more data are needed for NGC 6342 to determine if this cluster also follows the same light element pattern. The lack of additional abundance correlations in NGC 6366 (e.g., Mg–Si correlation) indicates that the mechanism responsible for the O–Na anti-correlation did not reach temperatures high enough to significantly deplete Mg nor produce Si.

Although [O/Fe] is significantly enhanced ($[\text{O}/\text{Fe}] > +0.50$) for most stars in our sample, the heavier α -elements have a more modest enhancement of $\langle [\alpha/\text{Fe}] \rangle = +0.31$ ($\sigma = 0.06$). The Fe-peak elements Cr and Ni mostly track Fe, but there is some weak evidence that NGC 6366 may be slightly more enhanced in [Cr/Fe] and [Ni/Fe] than NGC 6342. Interestingly, NGC 6342 and NGC 6366 are both moderately enhanced in La with $\langle [\text{La}/\text{Fe}] \rangle \sim +0.20$, which likely indicates some enrichment via the main s-process. When the abundance patterns of NGC 6342 and NGC 6366 are compared with those of other similar metal-rich ($[\text{Fe}/\text{H}] > -1$) bulge clusters, we find that most metal-rich clusters share a common composition pattern. However, we find some evidence favoring significant cluster-to-cluster variations in [La/Fe], which could be an indication that inner Galaxy globular cluster formation was a more heterogeneous process than is reflected in the α -element chemistry.

A further comparison between metal-rich bulge globular clusters and bulge field stars with $[\text{Fe}/\text{H}] < -0.4$ indicates that both populations exhibit nearly identical $[\alpha/\text{Fe}]$, [Cr/Fe], and [Ni/Fe] abundance trends. However, the clusters are distinguished from the field stars by exhibiting larger [O/Fe] and [Na/Fe] dispersions, and also by their enhanced [La/Fe] abundances (for some clusters). At $[\text{Fe}/\text{H}] > -0.4$, the most metal-rich globular clusters may be further distinguished from the bulge field stars by remaining enhanced in $[\alpha/\text{Fe}]$ up to at least solar metallicity.

This paper uses data products produced by the OIR Telescope Data Center, supported by the Smithsonian Astrophysical Observatory. This research has made use of NASA’s Astrophysics Data System Bibliographic Services. This publication has made use of data products from the Two Micron All Sky Survey, which is a joint project of the University of Massachusetts and the Infrared Processing and Analysis Center/California Institute of

Technology, funded by the National Aeronautics and Space Administration and the National Science Foundation. The Second Palomar Observatory Sky Survey (POSS-II) was made by the California Institute of Technology with funds from the National Science Foundation, the National Geographic Society, the Sloan Foundation, the Samuel Oschin Foundation, and the Eastman Kodak Corporation. C.I.J. gratefully acknowledges support from the Clay Fellowship, administered by the Smithsonian Astrophysical Observatory. R.M.R. acknowledges support from the National Science Foundation (AST-1413755 and AST-1412673). C.A.P. gratefully acknowledges support from the Daniel Kirkwood Research Fund at Indiana University and from the National Science Foundation (AST-1412673).

REFERENCES

- Alonso, A., Salaris, M., Martinez-Roger, C., Straniero, O., & Arribas, S. 1997, *A&A*, 323, 374
- Alonso-García, J., Mateo, M., Sen, B., et al. 2012, *AJ*, 143, 70
- Alves-Brito, A., Barbuy, B., Zoccali, M., et al. 2006, *A&A*, 460, 269
- Alves-Brito, A., Meléndez, J., Asplund, M., Ramírez, I., & Yong, D. 2010, *A&A*, 513, AA35
- Arnould, M., Goriely, S., & Jorissen, A. 1999, *A&A*, 347, 572
- Barbuy, B., Zoccali, M., Ortolani, S., et al. 2006, *A&A*, 449, 349
- Barbuy, B., Zoccali, M., Ortolani, S., et al. 2009, *A&A*, 507, 405
- Bellini, A., Piotto, G., Milone, A. P., et al. 2013, *ApJ*, 765, 32
- Bensby, T., Adén, D., Meléndez, J., et al. 2011, *A&A*, 533, A134
- Bensby, T., Yee, J. C., Feltzing, S., et al. 2013, *A&A*, 549, A147
- Bershady, M., Barden, S., Blanche, P.-A., et al. 2008, *Proc. SPIE*, 7014, 70140H
- Bica, E., Bonatto, C., Barbuy, B., & Ortolani, S. 2006, *A&A*, 450, 105
- Busso, M., Gallino, R., & Wasserburg, G. J. 1999, *ARA&A*, 37, 239
- Campos, F., Kepler, S. O., Bonatto, C., & Ducati, J. R. 2013, *MNRAS*, 433, 243
- Carretta, E., Cohen, J. G., Gratton, R. G., & Behr, B. B. 2001, *AJ*, 122, 1469

- Carretta, E., Gratton, R. G., Bragaglia, A., Bonifacio, P., & Pasquini, L. 2004, *A&A*, 416, 925
- Carretta, E., Bragaglia, A., Gratton, R. G., et al. 2007, *A&A*, 464, 967
- Carretta, E., Bragaglia, A., Gratton, R. G., et al. 2009a, *A&A*, 505, 117
- Carretta, E., Bragaglia, A., Gratton, R., & Lucatello, S. 2009b, *A&A*, 505, 139
- Carretta, E., Bragaglia, A., Gratton, R. G., et al. 2014, *A&A*, 564, A60
- Carretta, E. 2015, *ApJ*, 810, 148
- Casetti-Dinescu, D. I., Girard, T. M., Korchagin, V. I., van Altena, W. F., & López, C. E. 2010, *AJ*, 140, 1282
- Castelli, F., & Kurucz, R. L. 2004, arXiv:astro-ph/0405087
- Cohen, J. G., Gratton, R. G., Behr, B. B., & Carretta, E. 1999, *ApJ*, 523, 739
- Cohen, J. G., & Kirby, E. N. 2012, *ApJ*, 760, 86
- Cordero, M. J., Pilachowski, C. A., Johnson, C. I., et al. 2014, *ApJ*, 780, 94
- Cordero, M. J., Pilachowski, C. A., Johnson, C. I., & Vesperini, E. 2015, *ApJ*, 800, 3
- Côté, P. 1999, *AJ*, 118, 406
- Da Costa, G. S., & Seitzer, P. 1989, *AJ*, 97, 405
- Da Costa, G. S., & Armandroff, T. E. 1995, *AJ*, 109, 2533
- D’Orazi, V., Gratton, R., Lucatello, S., et al. 2010, *ApJ*, 719, L213
- Dotter, A., Chaboyer, B., Jevremović, D., et al. 2008, *ApJS*, 178, 89
- Dotter, A., Sarajedini, A., Anderson, J., et al. 2010, *ApJ*, 708, 698
- Dubath, P., Meylan, G., & Mayor, M. 1997, *A&A*, 324, 505
- Feltzing, S., Primas, F., & Johnson, R. A. 2009, *A&A*, 493, 913
- Ferraro, F. R., Dalessandro, E., Mucciarelli, A., et al. 2009, *Nature*, 462, 483
- Forbes, D. A., & Bridges, T. 2010, *MNRAS*, 404, 1203
- Freeman, K. C., & Norris, J. 1981, *ARA&A*, 19, 319

- González Hernández, J. I., & Bonifacio, P. 2009, A&A, 497, 497
- Gonzalez, O. A., Rejkuba, M., Zoccali, M., et al. 2011, A&A, 530, A54
- Gratton, R., Sneden, C., & Carretta, E. 2004, ARA&A, 42, 385
- Gratton, R. G., Carretta, E., & Bragaglia, A. 2012, A&A Rev., 20, 50
- Gratton, R. G., Lucatello, S., Bragaglia, A., et al. 2006, A&A, 455, 271
- Gratton, R. G., Lucatello, S., Bragaglia, A., et al. 2007, A&A, 464, 953
- Harris, W. E. 1996, AJ, 112, 1487
- Heitsch, F., & Richtler, T. 1999, A&A, 347, 455
- Hill, V., Lecureur, A., Gómez, A., et al. 2011, A&A, 534, A80
- Hinkle, K., Wallace, L., Valenti, J., & Harmer, D. 2000, Visible and Near Infrared Atlas of the Arcturus Spectrum 3727-9300 Å ed. Kenneth Hinkle, Lloyd Wallace, Jeff Valenti, and Dianne Harmer. (San Francisco: ASP) ISBN: 1-58381-037-4, 2000
- James, G., François, P., Bonifacio, P., et al. 2004, A&A, 427, 825
- Johnson, H. R., Mould, J. R., & Bernat, A. P. 1982, ApJ, 258, 161
- Johnson, C. I., & Pilachowski, C. A. 2010, ApJ, 722, 1373
- Johnson, C. I., Rich, R. M., Fulbright, J. P., Valenti, E., & McWilliam, A. 2011, ApJ, 732, 108
- Johnson, C. I., Rich, R. M., Kobayashi, C., & Fulbright, J. P. 2012, ApJ, 749, 175
- Johnson, C. I., Rich, R. M., Kobayashi, C., et al. 2013, ApJ, 765, 157
- Johnson, C. I., Rich, R. M., Kobayashi, C., Kunder, A., & Koch, A. 2014, AJ, 148, 67
- Johnson, C. I., Rich, R. M., Pilachowski, C. A., et al. 2015, AJ, 150, 63
- Knezeck, P. M., Bershady, M. A., Willmarth, D., et al. 2010, Proc. SPIE, 7735, 77357D
- Kraft, R. P. 1994, PASP, 106, 553
- Kunder, A., Koch, A., Rich, R. M., et al. 2012, AJ, 143, 57
- Langer, G. E., Hoffman, R., & Sneden, C. 1993, PASP, 105, 301

- Lawler, J. E., Bonvallet, G., & Sneden, C. 2001, ApJ, 556, 452
- Marín-Franch, A., Aparicio, A., Piotto, G., et al. 2009, ApJ, 694, 1498
- Mauro, F., Moni Bidin, C., Cohen, R., et al. 2012, ApJ, 761, L29
- McWilliam, A., & Rich, R. M. 1994, ApJS, 91, 749
- McWilliam, A., Fulbright, J., & Rich, R. M. 2010, IAU Symposium, 265, 279
- Meléndez, J., Barbuy, B., Bica, E., et al. 2003, A&A, 411, 417
- Meléndez, J., Asplund, M., Alves-Brito, A., et al. 2008, A&A, 484, L21
- Minniti, D. 1995, AJ, 109, 1663
- Nataf, D. M., Gould, A. P., Pinsonneault, M. H., & Udalski, A. 2013, ApJ, 766, 77
- Ness, M., Freeman, K., Athanassoula, E., et al. 2013, MNRAS, 432, 2092
- O'connell, J. E., Johnson, C. I., Pilachowski, C. A., & Burks, G. 2011, PASP, 123, 1139
- Origlia, L., Valenti, E., & Rich, R. M. 2005a, MNRAS, 356, 1276
- Origlia, L., Valenti, E., Rich, R. M., & Ferraro, F. R. 2005b, MNRAS, 363, 897
- Origlia, L., Valenti, E., & Rich, R. M. 2008, MNRAS, 388, 1419
- Origlia, L., Rich, R. M., Ferraro, F. R., et al. 2011, ApJ, 726, L20
- Origlia, L., Massari, D., Rich, R. M., et al. 2013, ApJ, 779, L5
- Ortolani, S., Bica, E., & Barbuy, B. 1997, MNRAS, 284, 692
- Ortolani, S., Barbuy, B., Momany, Y., et al. 2011, ApJ, 737, 31
- Paust, N. E. Q., Aparicio, A., Piotto, G., et al. 2009, AJ, 137, 246
- Piotto, G., Milone, A. P., Bedin, L. R., et al. 2015, AJ, 149, 91
- Prantzos, N., Charbonnel, C., & Iliadis, C. 2007, A&A, 470, 179
- Ramírez, I., & Allende Prieto, C. 2011, ApJ, 743, 135
- Rich, R. M., Sosin, C., Djorgovski, S. G., et al. 1997, ApJ, 484, L25
- Roederer, I. U., & Thompson, I. B. 2015, MNRAS, 449, 3889

- Rossi, L. J., Ortolani, S., Barbuy, B., Bica, E., & Bonfanti, A. 2015, MNRAS, 450, 3270
- Rutledge, G. A., Hesser, J. E., Stetson, P. B., et al. 1997, PASP, 109, 883
- Ryde, N., Gustafsson, B., Edvardsson, B., et al. 2010, A&A, 509, A20
- Sarajedini, A., Bedin, L. R., Chaboyer, B., et al. 2007, AJ, 133, 1658
- Saviane, I., da Costa, G. S., Held, E. V., et al. 2012, A&A, 540, A27
- Skrutskie, M. F., Cutri, R. M., Stiening, R., et al. 2006, AJ, 131, 1163
- Sneden, C. 1973, ApJ, 184, 839
- Sneden, C., Cowan, J. J., & Gallino, R. 2008, ARA&A, 46, 241
- Sneden, C., Lucatello, S., Ram, R. S., Brooke, J. S. A., & Bernath, P. 2014, ApJS, 214, 26
- Szentgyorgyi, A., Furesz, G., Cheimets, P., et al. 2011, PASP, 123, 1188
- Tinsley, B. M. 1979, ApJ, 229, 1046
- Valenti, E., Ferraro, F. R., & Origlia, L. 2004, MNRAS, 351, 1204
- Valenti, E., Origlia, L., & Rich, R. M. 2011, MNRAS, 414, 2690
- VandenBerg, D. A., Brogaard, K., Leaman, R., & Casagrande, L. 2013, ApJ, 775, 134
- van den Bergh, S. 2003, ApJ, 590, 797
- Ventura, P., D'Antona, F., Di Criscienzo, M., et al. 2012, ApJ, 761, L30
- Worley, C. C., & Cottrell, P. L. 2010, MNRAS, 406, 2504
- Yong, D., Grundahl, F., Nissen, P. E., Jensen, H. R., & Lambert, D. L. 2005, A&A, 438, 875
- Yong, D., Roederer, I. U., Grundahl, F., et al. 2014, MNRAS, 441, 3396
- Zinn, R. 1985, ApJ, 293, 424
- Zoccali, M., Gonzalez, O. A., Vasquez, S., et al. 2014, A&A, 562, A66

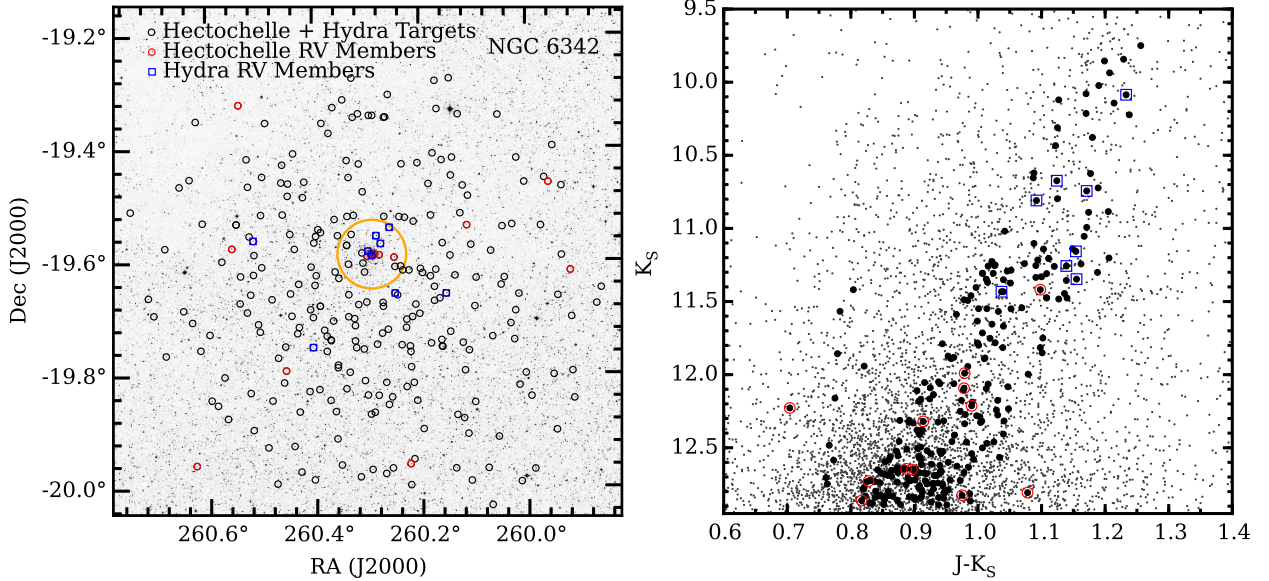


Fig. 1.— *left:* A Second Palomar Observatory Sky Survey r–band image of NGC 6342 is shown, and the open black circles designate the coordinates of all stars observed with MMT–Hectochelle and WIYN–Hydra. The open red circles (Hectochelle) and open blue boxes (Hydra) indicate the stars that have radial velocities consistent with cluster membership. The solid orange contour line illustrates a distance of 5 times the cluster’s 0.73’ half–light radius (Harris 1996; 2010 version). *right:* A K_S versus $J-K_S$ color–magnitude diagram is shown for targets within 30’ of NGC 6342. The small filled grey circles are all of the stars from the 2MASS database (Skrutskie et al. 2006). The red and blue symbols are the same as in the left panel, and the filled black circles indicate all stars that were observed with both instruments. Note that the two stars 2MASS 17220959–1919193 and 2MASS 17223024–1957315 have velocities that may be consistent with cluster membership but are significantly bluer and redder than the main giant branch.

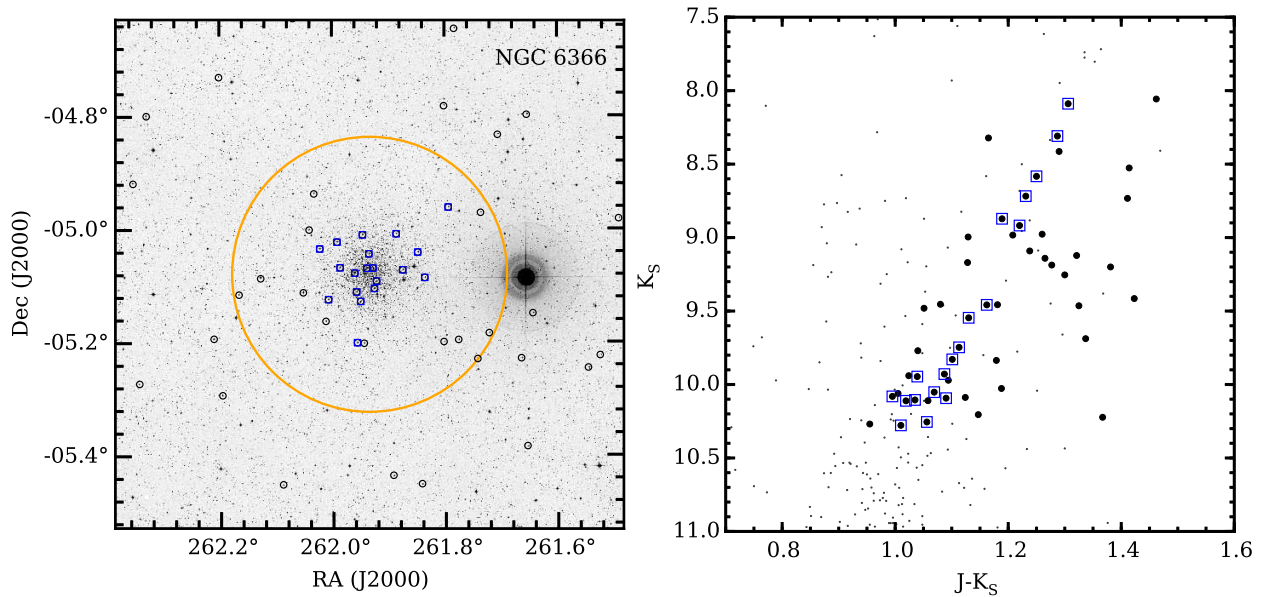


Fig. 2.— *left:* Similar to Figure 1, the open black circles show the coordinates for all stars near NGC 6366 that were observed with the WIYN–Hydra instrument. The targets that have radial velocities consistent with cluster membership are designated by open blue boxes. The solid orange contour line illustrates a distances of 5 times the cluster’s 2.92’ half-light radius (Harris 1996; 2010 version). *right:* A K_S versus J–K_S color–magnitude diagram is shown for targets within 30’ of NGC 6366. The small filled grey circles are all stars from the 2MASS database (Skrutskie et al. 2006). The black and blue symbols are the same as those in Figure 1.

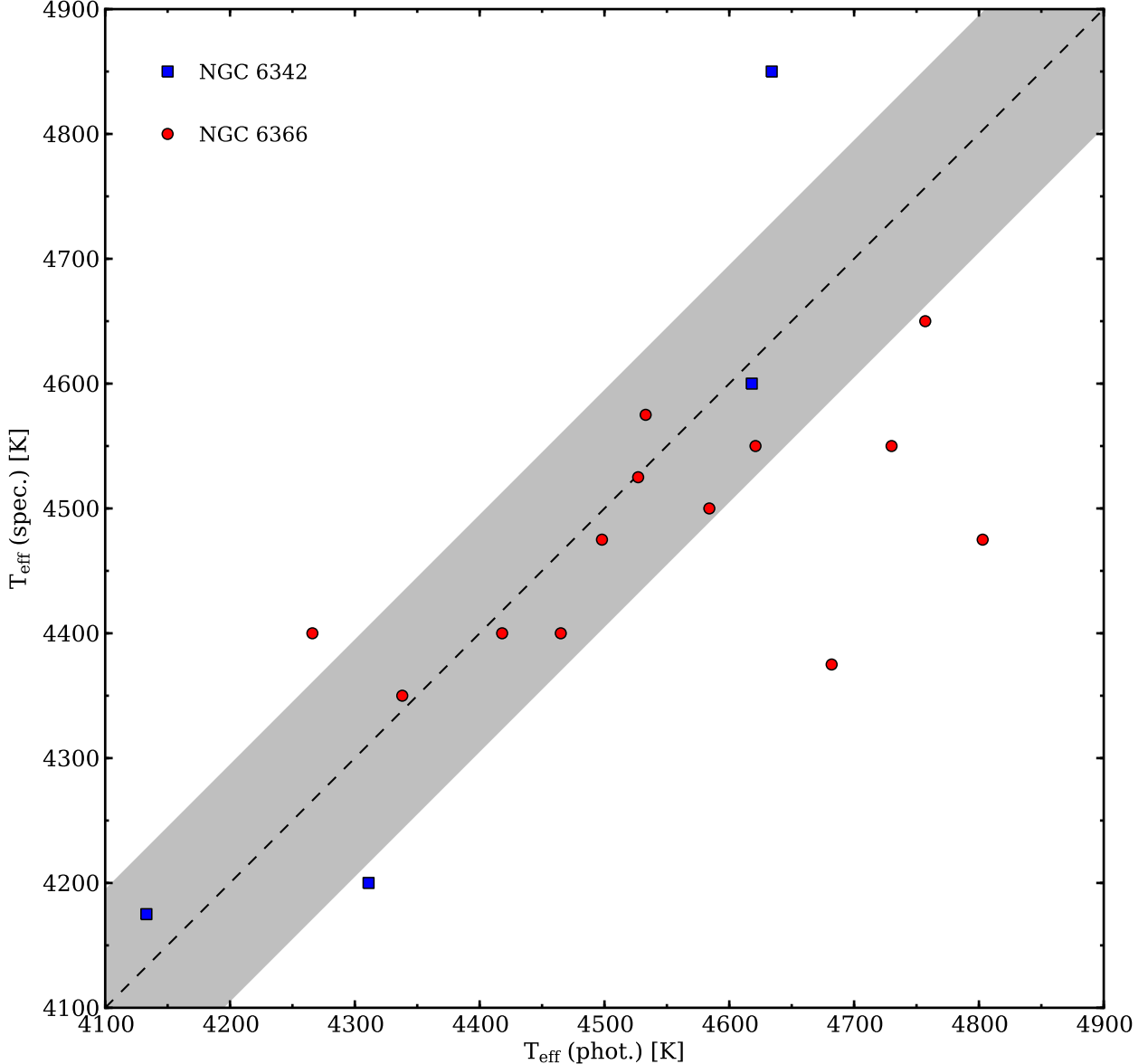


Fig. 3.— A comparison between the effective temperatures derived by enforcing excitation equilibrium of Fe I ($T_{\text{eff}} \text{ spec.}$) and using the $J-K_S$ color–temperature relation ($T_{\text{eff}} \text{ phot.}$) from González Hernández & Bonifacio (2009) for NGC 6342 (filled red circles) and NGC 6366 (filled blue boxes). The dashed black line indicates perfect agreement, and the shaded region illustrates the 1σ temperature uncertainty from González Hernández & Bonifacio (2009).

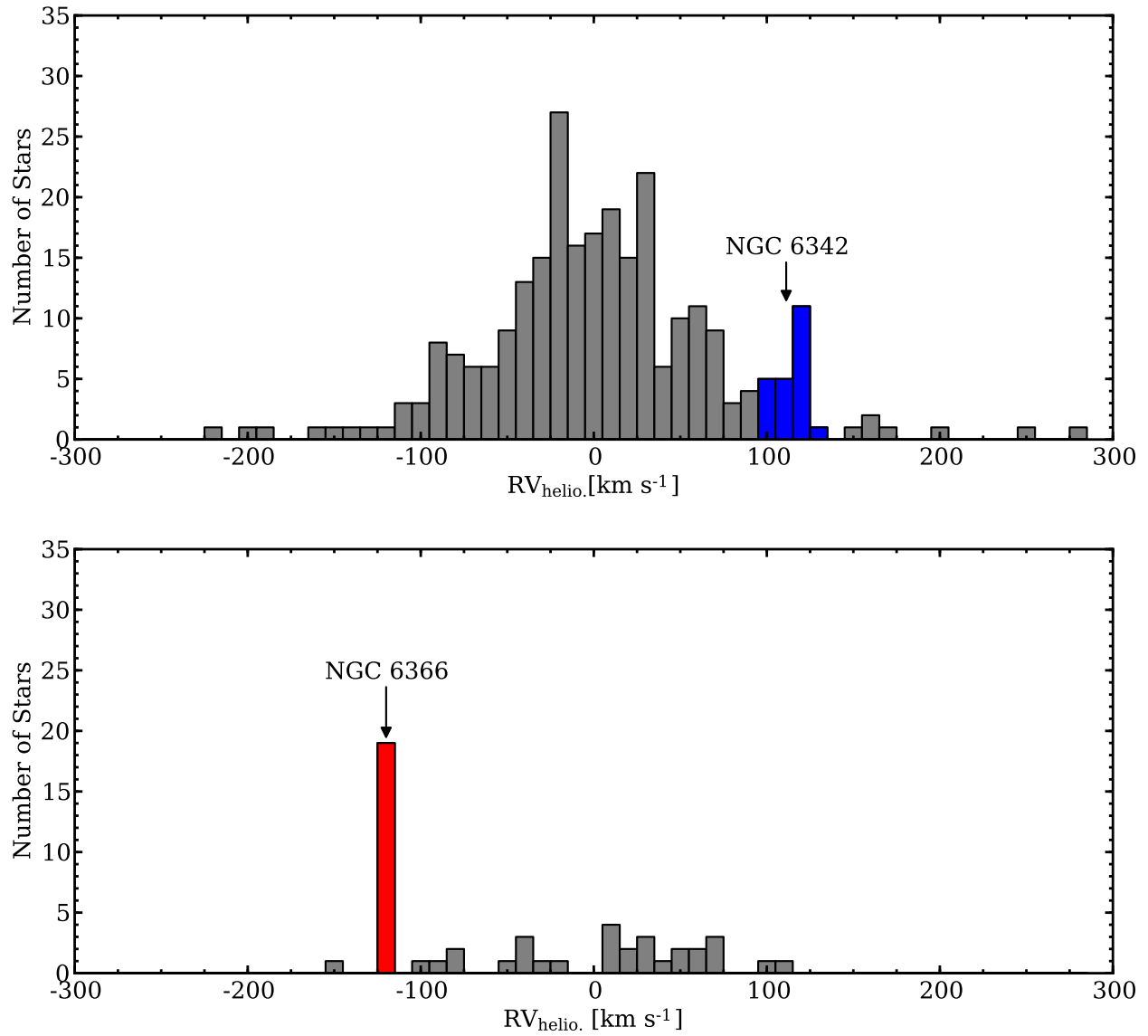


Fig. 4.— The heliocentric radial velocity distributions for the fields near NGC 6342 (top) and NGC 6366 (bottom) are shown with bin sizes of 10 km s^{-1} . The high probability members for each cluster are highlighted in blue for NGC 6342 and red for NGC 6366.

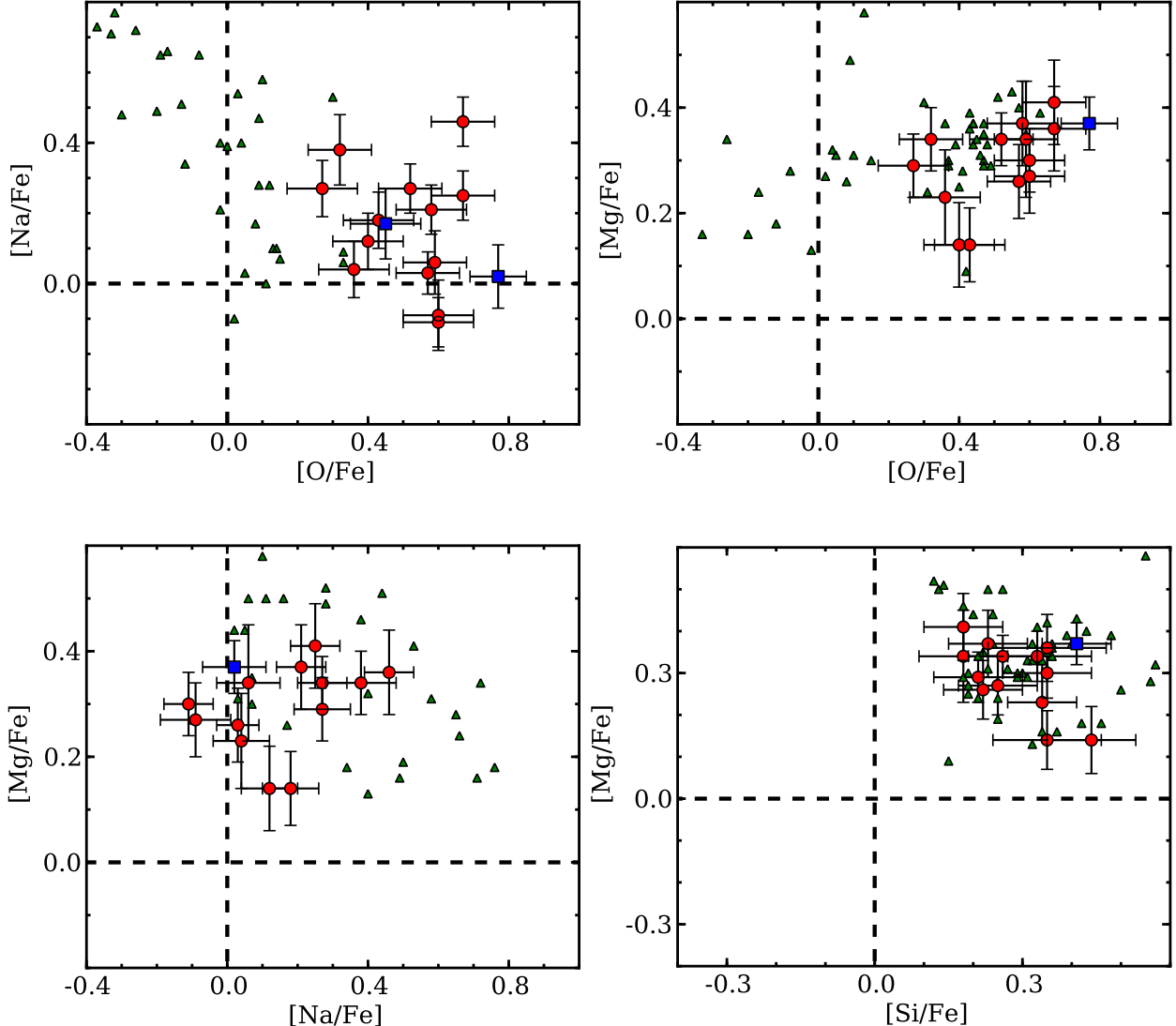


Fig. 5.— Similar to Figure 11 of Carretta (2015), plots of the O–Na, O–Mg, Na–Mg, and Si–Mg distributions are shown for NGC 6342 and NGC 6366. The dashed black lines indicate the solar abundances ratios, and the symbols are the same as those in Figure 3. The filled green triangles in each panel indicate the abundance ratios for individual stars of the bulge globular clusters listed in Table 7. For comparison purposes we have only included clusters that have $[\text{Fe}/\text{H}]$ between -0.70 and -0.40 , which are comparable to the metallicities of NGC 6342 and NGC 6366.

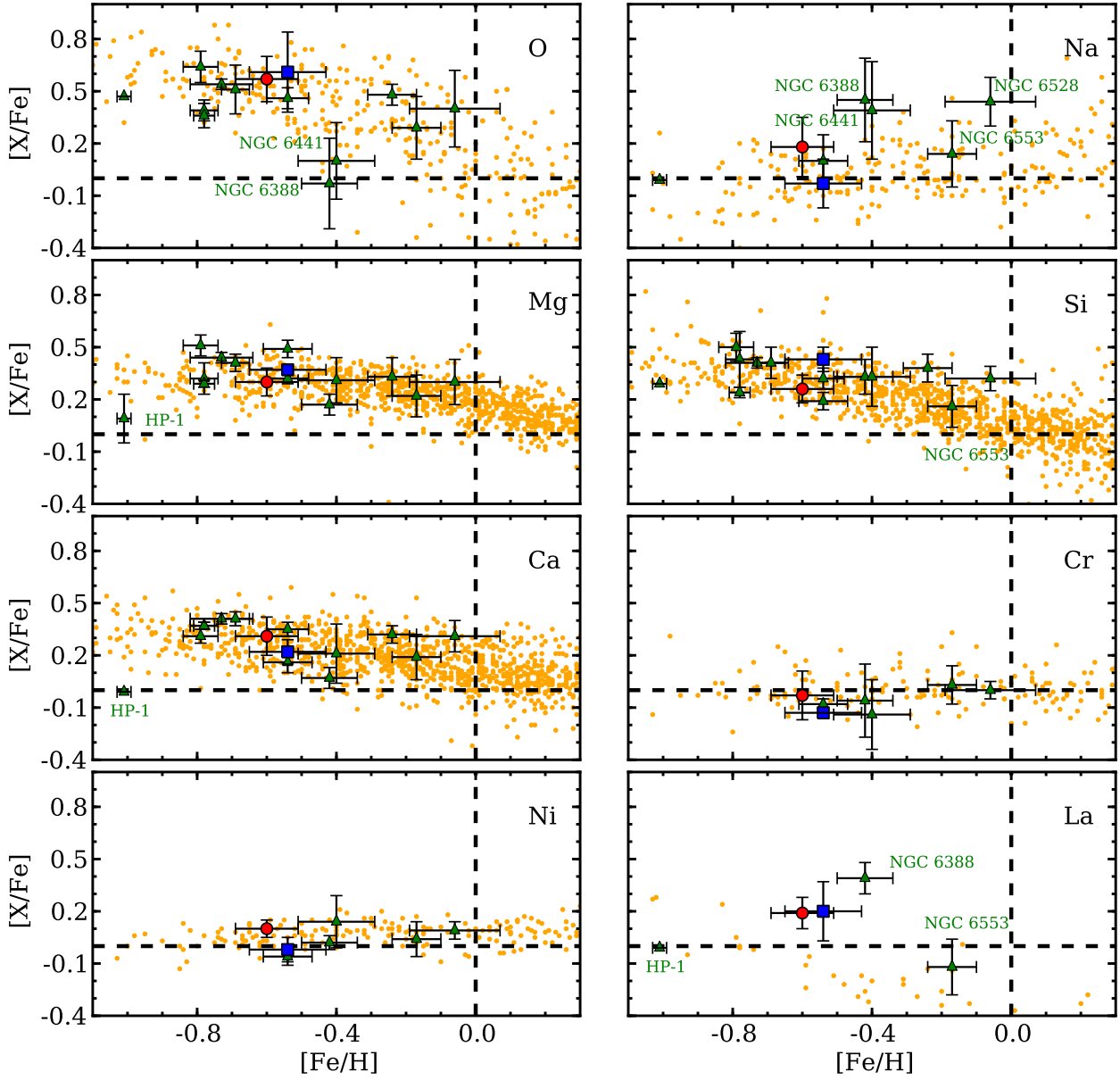


Fig. 6.— The panels compare the $[X/\text{Fe}]$ ratios of NGC 6342 (filled blue squares) and NGC 6366 (filled red circles) as a function of $[\text{Fe}/\text{H}]$ with bulge field star (filled orange circles) and bulge globular cluster (filled green triangles) data from the literature. The bulge globular cluster data are limited to those having $-1 \lesssim [\text{Fe}/\text{H}] \lesssim 0$ and a Galactocentric distance (R_{GC}) $\lesssim 5$ kpc. For all clusters, the symbols indicate the median abundance ratios and the error bars show the standard deviation. The literature references are provided in Table 7. Clusters of interest in each panel are identified by name (see text for details). For Terzan 5, only stars with $[\text{Fe}/\text{H}] < 0$ have been included, and the metal-poor ($[\text{Fe}/\text{H}] \sim -0.8$) and intermediate metallicity ($[\text{Fe}/\text{H}] \sim -0.3$) populations are shown as separate symbols.

Table 1. NGC 6342 Coordinates, Photometry, and Velocities

Star Name (2MASS)	RA (J2000) (Degrees)	DEC (J2000) (Degrees)	J (mag.)	H (mag.)	K _S (mag.)	RV _{helio.} (km s ⁻¹)	RV Error (km s ⁻¹)
Hectochelle Probable Members							
17194058–1937038	259.919111	−19.617743	13.531	12.862	12.644	+102.06	0.30
17195030–1927431	259.959610	−19.461985	13.234	12.509	12.320	+121.84	0.26
17202716–1932143	260.113200	−19.537306	13.800	13.046	12.825	+110.83	0.49
17205345–1957303	260.222729	−19.958424	12.477	11.643	11.493	+95.49	0.22
17210009–1935354	260.250404	−19.593189	12.517	11.700	11.419	+121.35	0.24
17210680–1935191	260.278335	−19.588644	13.071	12.292	12.093	+112.73	0.31
17210888–1935147	260.287009	−19.587433	13.678	13.014	12.861	+117.16	0.43
17211070–1935147	260.294586	−19.587420	13.545	12.936	12.649	+119.93	0.53
17211222–1935291	260.300920	−19.591421	13.203	12.510	12.213	+115.39	0.32
17214926–1947318	260.455264	−19.792168	13.556	12.856	12.728	+102.01	0.43
17220959–1919193	260.539973	−19.322044	13.885	13.066	12.807	+99.59	1.06
17221321–1934325	260.555060	−19.575714	12.969	12.175	11.990	+120.55	0.27
17223024–1957315	260.626001	−19.958773	12.932	12.347	12.228	+105.08	0.32
Hectochelle Probable Non-Members							
17192669–1938549	259.861219	−19.648594	13.622	12.915	12.721	−67.94	0.33
17192877–1940358	259.869892	−19.676620	13.553	12.978	12.723	−15.17	0.27
17193913–1950376	259.913066	−19.843796	12.223	11.535	11.419	−173.25	0.33
17193986–1947439	259.916084	−19.795542	12.277	11.526	11.250	−44.77	0.29
17194015–1941590	259.917329	−19.699745	12.600	11.804	11.568	−2.47	0.28
17194441–1928060	259.935070	−19.468357	13.593	12.913	12.626	−45.04	0.32
17194455–1935278	259.935628	−19.591057	13.712	12.995	12.782	+51.12	0.26
17194631–1939438	259.942995	−19.662176	13.493	12.830	12.651	+60.64	0.30
17194709–1953597	259.946240	−19.899942	13.423	12.791	12.561	+15.20	0.31
17194833–1923503	259.951416	−19.397331	12.826	12.054	11.873	+14.80	0.20
17194834–1948062	259.951444	−19.801746	13.289	12.612	12.378	+11.26	0.35
17195217–1927124	259.967399	−19.453459	13.510	12.770	12.637	+64.17	0.27
17195386–1932185	259.974422	−19.538490	13.636	12.966	12.797	−2.61	0.31
17195710–1958071	259.987920	−19.968639	12.466	11.663	11.488	+92.36	0.23
17195849–1950235	259.993709	−19.839867	13.558	12.895	12.734	+34.86	0.23
17200094–1947559	260.003947	−19.798882	12.936	12.319	12.161	−0.02	0.25
17200119–1927409	260.004979	−19.461382	13.731	12.988	12.858	−222.21	0.65
17200325–1959267	260.013568	−19.990774	12.636	12.013	11.857	−23.40	0.21
17200383–1949125	260.015992	−19.820152	12.602	11.778	11.550	−18.30	0.27
17200391–1939333	260.016309	−19.659252	13.204	12.527	12.312	−77.76	0.29
17200465–1925073	260.019413	−19.418722	13.608	12.950	12.735	+9.54	0.36
17200541–1941188	260.022577	−19.688566	13.678	12.986	12.831	−67.42	0.43
17200601–1944228	260.025057	−19.739676	13.535	12.905	12.682	−25.42	0.25
17200681–1932100	260.028386	−19.536121	13.315	12.535	12.336	+89.66	0.34
17200762–1942402	260.031790	−19.711184	13.620	12.922	12.689	−7.22	0.32
17201041–1937471	260.043377	−19.629772	13.526	12.847	12.615	−1.74	0.31
17201186–1938344	260.049441	−19.642895	13.674	12.931	12.746	+29.12	0.36
17201294–1920323	260.053921	−19.342319	13.678	12.986	12.741	+30.09	0.32
17201342–1954417	260.055927	−19.911585	12.274	11.534	11.258	−22.70	0.23
17201592–1944023	260.066363	−19.733978	12.495	11.649	11.356	−14.71	0.38

Table 1—Continued

Star Name (2MASS)	RA (J2000) (Degrees)	DEC (J2000) (Degrees)	J (mag.)	H (mag.)	K _S (mag.)	RV _{helio.} (km s ⁻¹)	RV Error (km s ⁻¹)
17201656–2001560	260.069029	−20.032248	13.307	12.555	12.276	−15.65	0.31
17201818–1958002	260.075772	−19.966728	13.417	12.709	12.458	+30.73	0.30
17202381–1940495	260.099231	−19.680441	12.563	11.775	11.549	−24.78	0.21
17202393–1950597	260.099730	−19.849943	13.519	12.827	12.655	+59.11	0.26
17202536–1934185	260.105708	−19.571814	12.401	11.590	11.404	−13.20	0.22
17202587–1959192	260.107800	−19.988670	12.554	11.773	11.588	−186.46	0.25
17202650–1945302	260.110432	−19.758400	13.090	12.428	12.166	−93.73	0.27
17202717–1954207	260.113223	−19.905752	13.318	12.641	12.410	−15.98	0.32
17202836–1947377	260.118180	−19.793812	13.596	12.890	12.677	−0.33	0.24
17202890–1928013	260.120424	−19.467030	13.676	12.995	12.720	+6.67	0.43
17202903–1952412	260.120978	−19.878136	13.619	12.919	12.725	−197.44	0.34
17203084–1920274	260.128525	−19.340967	13.798	13.014	12.872	−16.72	0.40
17203202–1952211	260.133456	−19.872538	13.828	13.074	12.890	+31.95	0.24
17203287–1958005	260.136992	−19.966810	12.383	11.560	11.368	+67.02	0.36
17203363–1925030	260.140136	−19.417503	13.742	13.009	12.789	−2.57	0.31
17203422–1926568	260.142600	−19.449112	13.024	12.239	12.062	−106.07	0.36
17203468–1916379	260.144507	−19.277214	13.667	13.011	12.747	−25.50	0.35
17203485–1943309	260.145247	−19.725267	13.698	13.015	12.832	+24.77	0.32
17203825–1934067	260.159379	−19.568529	13.523	12.823	12.642	+70.73	0.32
17203875–1945043	260.161478	−19.751204	12.849	12.139	11.891	−42.01	0.28
17203889–1944226	260.162082	−19.739637	12.771	11.965	11.752	+33.21	0.22
17203957–1939576	260.164897	−19.666012	13.223	12.470	12.251	+25.22	0.28
17204035–1919530	260.168128	−19.331398	12.408	11.442	11.202	−90.75	0.28
17204113–1916533	260.171412	−19.281488	13.262	12.533	12.316	−48.48	0.27
17204129–1936548	260.172077	−19.615242	12.489	11.568	11.301	+13.79	0.26
17204195–1938438	260.174820	−19.645512	12.844	12.046	11.882	+74.29	0.24
17204237–1924343	260.176579	−19.409550	13.852	13.117	12.864	−57.67	0.37
17204339–1931097	260.180814	−19.519388	13.324	12.505	12.318	+2.89	0.33
17204360–1944436	260.181667	−19.745449	13.547	12.896	12.689	−98.16	0.33
17204374–1937366	260.182267	−19.626841	13.648	12.878	12.670	−100.61	0.30
17204438–1927492	260.184931	−19.463688	13.544	12.833	12.670	+33.23	0.58
17204731–1937150	260.197155	−19.620840	13.405	12.697	12.495	−8.60	0.34
17204737–1953483	260.197402	−19.896757	13.229	12.475	12.331	+19.21	0.25
17204822–1936487	260.200942	−19.613537	13.568	12.855	12.667	+46.87	0.30
17204874–1941343	260.203120	−19.692863	13.279	12.488	12.281	+2.95	0.24
17205014–1950474	260.208926	−19.846519	13.262	12.574	12.325	−26.47	0.35
17205047–1940358	260.210316	−19.676624	13.493	12.808	12.583	+59.80	0.36
17205126–1931479	260.213622	−19.529985	13.376	12.585	12.413	+278.60	0.39
17205158–1948535	260.214935	−19.814873	13.332	12.606	12.456	+28.55	0.23
17205172–1956596	260.215538	−19.949915	13.687	13.005	12.827	−12.20	0.33
17205198–1941546	260.216605	−19.698515	13.727	13.014	12.835	+35.55	0.31
17205293–1945365	260.220544	−19.760143	13.592	12.909	12.771	−20.29	0.31
17205317–1945010	260.221564	−19.750296	13.429	12.752	12.555	−51.54	0.32
17205330–1959442	260.222098	−19.995638	13.249	12.581	12.483	−50.19	0.26
17205340–1936577	260.222534	−19.616049	13.398	12.708	12.510	−6.84	0.35

Table 1—Continued

Star Name (2MASS)	RA (J2000) (Degrees)	DEC (J2000) (Degrees)	J (mag.)	H (mag.)	K _S (mag.)	RV _{helio.} (km s ⁻¹)	RV Error (km s ⁻¹)
17205462–1942107	260.227589	−19.702976	12.633	11.822	11.634	+26.84	0.35
17205480–1943031	260.228360	−19.717537	13.358	12.773	12.585	+45.18	0.27
17205483–1949197	260.228493	−19.822151	13.002	12.263	12.062	−53.58	0.31
17205518–1931224	260.229952	−19.522907	13.643	12.869	12.726	+18.38	0.38
17205620–1936570	260.234206	−19.615856	13.013	12.233	12.109	−25.43	0.24
17205642–1925420	260.235108	−19.428358	13.706	13.263	12.877	+68.23	0.51
17205688–1944533	260.237022	−19.748152	13.207	12.324	12.176	+32.45	1.67
17205703–2004175	260.237643	−20.071552	13.465	12.830	12.704	+23.79	0.30
17205715–1936317	260.238142	−19.608824	13.559	12.853	12.695	−22.97	0.28
17205764–1931174	260.240187	−19.521500	13.600	12.819	12.566	−30.23	0.40
17205865–1939355	260.244384	−19.659876	13.680	13.061	12.773	−15.14	0.56
17205971–1936344	260.248796	−19.609556	13.288	12.540	12.376	+8.02	0.25
17210143–1950243	260.255999	−19.840107	13.740	13.127	12.888	+35.36	0.28
17210147–1957562	260.256152	−19.965622	13.511	12.930	12.748	−23.86	0.33
17210222–1918201	260.259271	−19.305592	12.417	11.572	11.309	+24.19	0.31
17210297–1951122	260.262381	−19.853411	13.753	13.101	12.844	−39.86	0.25
17210303–1943136	260.262632	−19.720457	13.600	12.900	12.659	−0.92	0.36
17210413–1920441	260.267222	−19.345585	13.444	12.677	12.462	−30.48	0.35
17210455–1958310	260.268982	−19.975292	13.561	12.868	12.621	−28.84	0.33
17210512–1940473	260.271356	−19.679811	12.310	11.448	11.216	+8.13	0.30
17210526–1940225	260.271950	−19.672943	13.089	12.380	12.182	−90.80	0.22
17210565–1943381	260.273581	−19.727251	13.614	12.876	12.674	−36.29	0.32
17210752–1950133	260.281366	−19.837049	13.755	13.043	12.854	+8.49	0.28
17210798–1944480	260.283250	−19.746670	12.733	12.021	11.789	−37.42	0.23
17210937–1920314	260.289060	−19.342075	13.801	13.072	12.814	−106.74	0.38
17210937–1952010	260.289051	−19.866949	12.709	11.926	11.669	−6.26	0.27
17211069–1958044	260.294542	−19.967916	12.800	12.021	11.799	+12.96	0.25
17211091–1920313	260.295466	−19.342045	12.612	11.798	11.543	−60.21	0.27
17211110–1952125	260.296252	−19.870165	13.108	12.342	12.095	+27.07	0.25
17211237–1950107	260.301579	−19.836317	13.715	13.071	12.881	+161.90	0.35
17211260–1940190	260.302505	−19.671967	12.970	12.265	12.054	+70.92	0.22
17211346–1937077	260.306116	−19.618828	13.570	12.882	12.732	−53.72	0.36
17211365–1948387	260.306893	−19.810772	13.589	12.876	12.674	+7.63	0.35
17211399–1945176	260.308319	−19.754894	13.586	12.926	12.740	−23.56	0.31
17211457–1935059	260.310717	−19.584993	13.709	12.937	12.764	−87.90	0.26
17211567–1925399	260.315300	−19.427755	13.546	12.835	12.644	−5.09	0.37
17211579–1920207	260.315820	−19.339090	13.449	12.756	12.595	+28.27	0.45
17211604–1958507	260.316866	−19.980768	13.470	12.684	12.525	−1.61	0.28
17211625–1940345	260.317715	−19.676260	12.550	11.729	11.549	−116.56	0.22
17211742–1945086	260.322603	−19.752401	13.396	12.759	12.524	−85.73	0.32
17211786–1942484	260.324441	−19.713463	13.584	12.856	12.681	+64.33	0.26
17211791–1944255	260.324638	−19.740423	13.696	12.956	12.724	−23.85	0.31
17211818–1942038	260.325764	−19.701065	13.441	12.728	12.581	−27.01	0.29
17211853–1916328	260.327237	−19.275803	12.782	11.999	11.783	−60.06	0.42
17211928–1933077	260.330352	−19.552147	13.296	12.602	12.384	+15.96	0.30

Table 1—Continued

Star Name (2MASS)	RA (J2000) (Degrees)	DEC (J2000) (Degrees)	J (mag.)	H (mag.)	K _S (mag.)	RV _{helio.} (km s ⁻¹)	RV Error (km s ⁻¹)
17212066–1936171	260.336095	−19.604750	13.778	13.113	12.840	+253.12	2.20
17212068–1939312	260.336184	−19.658682	12.987	12.251	12.049	−5.44	0.24
17212110–1931128	260.337920	−19.520243	13.736	13.016	12.810	−42.87	0.35
17212113–1925169	260.338052	−19.421383	13.553	12.787	12.600	+57.42	0.41
17212139–1934169 ^a	260.339162	−19.571383	12.314	11.522	11.307	+2.36	0.21
17212205–1949292	260.341878	−19.824793	13.540	12.813	12.613	+1.58	0.31
17212277–1918506	260.344898	−19.314058	13.716	12.975	12.804	−147.47	0.57
17212453–1957342	260.352217	−19.959501	13.468	12.784	12.542	−63.53	0.32
17212549–1933147	260.356213	−19.554100	12.897	12.120	11.886	−55.29	0.25
17212577–1946584	260.357394	−19.782894	13.076	12.279	11.997	+7.83	0.39
17212641–1954475	260.360066	−19.913216	13.596	12.924	12.706	−97.17	0.31
17212673–1937056	260.361379	−19.618248	13.671	13.009	12.825	−21.95	0.27
17212695–1951540	260.362309	−19.865021	13.214	12.547	12.323	−65.55	0.29
17212727–1919391	260.363638	−19.327541	13.484	12.698	12.470	−71.42	0.34
17212772–1942170	260.365508	−19.704741	13.482	12.749	12.540	−17.89	0.60
17212896–1944170	260.370675	−19.738064	13.576	12.818	12.669	−21.93	0.22
17212920–1922228	260.371674	−19.373022	12.852	11.980	11.750	−17.40	0.25
17212931–1950420	260.372135	−19.845011	13.842	13.128	12.891	−20.52	0.32
17213073–1945299	260.378043	−19.758329	13.331	12.608	12.327	−38.51	0.33
17213179–1943154	260.382474	−19.720964	12.952	12.112	11.851	−15.17	0.28
17213229–1921190	260.384576	−19.355305	13.447	12.679	12.407	−35.55	0.36
17213359–1940422 ^a	260.389966	−19.678402	12.250	11.498	11.228	+52.92	0.33
17213428–1932347	260.392844	−19.542984	13.081	12.280	12.065	+147.23	0.34
17213428–1949324	260.392865	−19.825682	13.519	12.841	12.672	+20.98	0.34
17213527–1937276	260.396978	−19.624346	13.410	12.704	12.505	+82.25	0.26
17213535–1933175	260.397293	−19.554869	13.678	13.030	12.840	−87.71	0.35
17213588–1938294	260.399500	−19.641527	13.710	13.066	12.878	+57.45	0.30
17213620–1933593	260.400870	−19.566496	13.150	12.443	12.176	+56.97	0.38
17213681–1941537	260.403383	−19.698273	13.600	12.921	12.658	−3.25	0.38
17213687–1959067	260.403634	−19.985216	12.338	11.555	11.292	−6.78	0.22
17213801–1941038	260.408391	−19.684408	13.508	12.749	12.501	−22.99	0.39
17213875–1949446	260.411475	−19.829069	13.706	13.099	12.853	+28.54	0.29
17213914–2003403	260.413099	−20.061220	13.078	12.406	12.168	+40.69	0.32
17214034–1927316	260.418101	−19.458784	13.358	12.583	12.317	−84.65	0.43
17214107–1929095	260.421147	−19.485977	13.617	12.843	12.632	−7.10	0.34
17214286–1958157	260.428624	−19.971031	13.766	13.140	12.888	+26.34	0.36
17214319–1942560	260.429993	−19.715557	13.178	12.397	12.187	+53.38	0.27
17214324–1938210	260.430182	−19.639181	13.564	12.935	12.728	−43.56	0.33
17214327–1951540	260.430295	−19.865026	13.673	12.981	12.743	−15.59	0.34
17214398–1943354	260.433275	−19.726515	12.901	12.156	11.891	−0.56	0.26
17214502–1934383	260.437585	−19.577307	13.291	12.503	12.288	+9.14	0.26
17214584–1955322	260.441008	−19.925638	13.271	12.466	12.242	−26.24	0.31
17214647–1941436	260.443641	−19.695459	13.640	12.922	12.753	+42.66	0.30
17214698–1933032	260.445753	−19.550915	13.653	13.006	12.830	+46.55	0.32
17214700–1939214	260.445845	−19.655970	13.472	12.787	12.564	−34.49	0.34

Table 1—Continued

Star Name (2MASS)	RA (J2000) (Degrees)	DEC (J2000) (Degrees)	J (mag.)	H (mag.)	K _S (mag.)	RV _{helio.} (km s ⁻¹)	RV Error (km s ⁻¹)
17214767–1927419	260.448636	−19.461641	13.253	12.529	12.273	+15.03	0.34
17214791–1929004	260.449653	−19.483463	13.015	12.352	12.090	+23.06	0.31
17215020–1948473	260.459183	−19.813160	12.449	11.681	11.460	+195.38	0.32
17215025–1930586	260.459411	−19.516294	12.338	11.525	11.286	−140.92	0.23
17215274–1946097	260.469781	−19.769363	12.928	12.138	11.944	+166.62	0.28
17215378–1959302	260.474088	−19.991728	13.603	12.946	12.783	+54.49	0.30
17215554–1950411	260.481430	−19.844772	13.190	12.518	12.313	+30.49	0.31
17215764–1955389	260.490197	−19.927483	13.698	12.999	12.787	+8.15	0.30
17215768–1921148	260.490369	−19.354113	13.083	12.307	12.106	−16.66	0.39
17220087–1943226	260.503649	−19.722956	13.751	13.036	12.804	+87.31	0.30
17220161–1942348	260.506713	−19.709694	12.722	11.960	11.715	−5.12	0.25
17220360–1937208	260.515012	−19.622456	13.658	13.027	12.799	−30.85	0.30
17220422–1953478	260.517594	−19.896614	13.440	12.744	12.520	+8.65	0.33
17220497–1939260	260.520711	−19.657248	13.690	12.961	12.746	+2.38	1.20
17220535–1949517	260.522326	−19.831038	13.465	12.715	12.525	−10.79	0.31
17220536–1933156	260.522334	−19.554342	13.467	12.747	12.559	−24.87	0.28
17220623–1925040	260.525982	−19.417786	12.809	12.026	11.782	−80.17	0.32
17220941–1937289	260.539223	−19.624699	13.530	12.804	12.540	−25.75	0.39
17220978–1940206	260.540764	−19.672413	13.066	12.355	12.136	−71.59	0.33
17221115–1931581 ^a	260.546495	−19.532812	12.583	11.710	11.475	+27.44	0.21
17221579–1952348	260.565816	−19.876337	13.626	12.911	12.691	−28.71	0.32
17221708–1948102	260.571187	−19.802839	12.425	11.633	11.374	+55.33	0.28
17221779–1935538	260.574161	−19.598288	12.854	12.065	11.815	+155.68	0.27
17222021–1951100	260.584248	−19.852785	13.791	13.129	12.845	−113.35	0.33
17222304–1950369	260.596018	−19.843597	13.130	12.354	12.083	−91.29	0.26
17222359–1943386	260.598299	−19.727390	13.739	13.107	12.840	−83.87	0.35
17222641–1931500	260.610063	−19.530565	12.913	12.077	11.815	+47.15	0.44
17222780–1945183	260.615868	−19.755096	13.515	12.860	12.642	+70.22	0.41
17222890–1921019	260.620446	−19.350554	12.763	12.161	11.942	+25.50	0.37
17223138–1942206	260.630788	−19.705727	13.283	12.564	12.379	−125.03	1.16
17223206–1927114	260.633603	−19.453180	13.688	13.066	12.836	−75.33	0.63
17223532–1941053	260.647189	−19.684830	13.666	12.955	12.758	−82.18	0.26
17223662–1927567	260.652614	−19.465775	12.350	11.736	11.567	−84.16	0.38
17224344–1934285	260.681014	−19.574606	13.282	12.498	12.234	+16.75	0.32
17224348–1945514	260.681206	−19.764290	12.677	11.868	11.655	−39.80	0.23
17224880–1941344	260.703367	−19.692913	13.748	13.050	12.837	+18.78	0.46
17225118–1939432	260.713283	−19.662014	13.572	12.873	12.579	−71.51	0.32
17225880–1930327	260.745003	−19.509094	13.758	13.040	12.811	+8.35	0.61
Hydra Probable Members							
17203668–1939270	260.152851	−19.657518	11.798	10.868	10.674	+110.01	0.28
17205974–1939237	260.248945	−19.656588	11.319	10.451	10.086	+98.28	0.71
17210211–1932252	260.258823	−19.540339	12.396	11.542	11.257	+113.28	0.66
17210615–1934073	260.275637	−19.568710	12.502	11.600	11.347	+117.27	0.43
17210813–1933174	260.283905	−19.554838	12.311	11.399	11.157	+115.40	0.87
17211015–1935227	260.292307	−19.589666	11.901	11.098	10.809	+126.56	0.29

Table 1—Continued

Star Name (2MASS)	RA (J2000) (Degrees)	DEC (J2000) (Degrees)	J (mag.)	H (mag.)	K _S (mag.)	RV _{helio.} (km s ⁻¹)	RV Error (km s ⁻¹)
17211185–1934551	260.299401	−19.581997	11.915	10.991	10.744	+115.25	0.30
17213696–1945045	260.404032	−19.751265	12.470	11.661	11.433	+116.28	0.30
17220360–1933439	260.515039	−19.562201	12.426	11.616	11.335	+119.50	0.62
Hydra Probable Non-Members							
17201119–1932228	260.046651	−19.539692	12.317	11.456	11.206	+32.13	0.40
17201643–1934577	260.068491	−19.582697	11.072	10.178	9.843	−16.76	0.27
17202313–1937485	260.096390	−19.630148	11.213	10.299	10.023	+27.19	0.48
17202663–1929066	260.110969	−19.485168	12.405	11.512	11.243	−61.52	0.53
17202927–1944416	260.121986	−19.744911	11.558	10.672	10.378	+31.90	0.52
17203014–1930574	260.125610	−19.515949	11.461	10.564	10.223	+13.95	0.43
17203482–1935256	260.145119	−19.590456	11.912	11.021	10.723	−9.88	0.50
17203834–1925180	260.159767	−19.421684	12.090	11.152	10.885	−89.51	1.47
17203848–1945061	260.160336	−19.751698	12.473	11.737	11.433	+55.49	0.73
17204202–1940132	260.175116	−19.670353	12.616	11.744	11.476	−46.53	0.43
17205272–1947140	260.219697	−19.787228	12.061	11.289	11.019	+40.73	0.50
17210354–1920423	260.264787	−19.345095	12.431	11.563	11.331	+68.03	0.24
17210404–1948513	260.266848	−19.814257	11.249	10.417	10.079	−47.61	1.06
17210448–1931152	260.268691	−19.520906	12.331	11.673	11.307	+6.37	0.38
17211406–1928370	260.308584	−19.476955	11.802	10.950	10.625	+24.99	0.37
17211414–1936108	260.308928	−19.603008	12.380	11.535	11.260	+5.47	0.46
17211816–1920425	260.325674	−19.345148	12.221	11.346	11.054	+22.97	0.46
17211820–1931065	260.325854	−19.518476	12.280	11.478	11.254	−20.44	0.31
17212036–1927053	260.334836	−19.451488	12.164	11.250	10.993	+40.02	0.48
17212047–1947445	260.335316	−19.795708	11.709	10.886	10.621	−43.53	0.20
17212084–1941512	260.336836	−19.697559	11.436	10.551	10.311	+70.53	0.41
17212139–1934169 ^a	260.339162	−19.571383	12.314	11.522	11.307	+1.25	0.22
17212508–1937461	260.354541	−19.629480	12.314	11.436	11.241	+22.87	0.28
17212583–1947142	260.357646	−19.787296	12.191	11.366	11.103	−13.98	0.45
17212689–1931313	260.362079	−19.525373	11.357	10.476	10.143	−23.77	0.83
17212880–1944224	260.370018	−19.739576	12.610	11.679	11.483	+7.67	0.31
17213067–1943533	260.377827	−19.731485	11.922	11.084	10.797	−41.75	0.31
17213310–1932538	260.387926	−19.548296	11.556	10.725	10.434	−34.14	0.63
17213359–1940422 ^a	260.389966	−19.678402	12.250	11.498	11.228	+46.82	0.35
17213753–1936323	260.406375	−19.608999	11.741	10.937	10.654	−6.15	0.43
17214524–1924304	260.438500	−19.408463	12.581	11.721	11.445	−155.32	0.30
17214945–1944587	260.456078	−19.749660	11.054	10.165	9.855	−44.25	0.41
17215025–1925417	260.459397	−19.428253	12.244	11.365	11.141	+82.48	0.32
17215072–1927350	260.461360	−19.459749	12.345	11.520	11.254	+51.74	0.73
17215536–1939570	260.480698	−19.665852	11.248	10.376	10.121	+90.28	0.24
17215932–1926573	260.497205	−19.449261	12.064	11.217	10.890	−1.66	0.58
17215984–1936324	260.499343	−19.609022	12.391	11.551	11.351	+68.20	0.26
17220005–1930599	260.500227	−19.516642	11.006	10.039	9.750	−48.17	0.57
17220327–1935141	260.513647	−19.587261	11.384	10.536	10.214	−32.14	0.59
17220575–1927591	260.523999	−19.466438	12.360	11.566	11.347	+55.41	0.65
17220656–1941191	260.527372	−19.688658	11.143	10.262	9.936	+75.73	0.65

Table 1—Continued

Star Name (2MASS)	RA (J2000) (Degrees)	DEC (J2000) (Degrees)	J (mag.)	H (mag.)	K _S (mag.)	RV _{helio.} (km s ⁻¹)	RV Error (km s ⁻¹)
17221115–1931581 ^a	260.546495	−19.532812	12.583	11.710	11.475	+27.26	0.28

^aThis flag indicates that the star was observed with both the Hectochelle and Hydra instruments.

Table 2. NGC 6366 Coordinates, Photometry, and Velocities

Star Name (2MASS)	RA (J2000) (Degrees)	DEC (J2000) (Degrees)	J (mag.)	H (mag.)	K _S (mag.)	RV _{helio.} (km s ⁻¹)	RV Error (km s ⁻¹)
Hydra Probable Members							
17271061–0457415	261.794225	−4.961547	11.016	10.189	9.929	−121.91	0.21
17272071–0505087	261.836299	−5.085757	11.288	10.482	10.278	−122.47	0.21
17272367–0502272	261.848632	−5.040897	10.138	9.200	8.918	−121.24	0.22
17273010–0504197	261.875443	−5.072152	10.860	9.994	9.747	−123.89	0.22
17273285–0500304	261.886891	−5.008450	11.140	10.316	10.105	−119.99	0.22
17274128–0505308	261.922036	−5.091896	11.311	10.506	10.255	−124.17	0.20
17274221–0506173	261.925909	−5.104828	10.061	9.131	8.872	−121.33	0.22
17274279–0504077	261.928333	−5.068811	10.930	10.041	9.829	−124.53	0.22
17274452–0502371	261.935500	−5.043651	10.985	10.157	9.946	−122.38	0.21
17274541–0504089	261.939246	−5.069143	11.121	10.283	10.052	−123.45	0.20
17274724–0500362	261.946845	−5.010075	10.620	9.714	9.458	−123.22	0.21
17274809–0507395	261.950399	−5.127661	11.183	10.296	10.093	−122.99	0.24
17274954–0512022	261.956422	−5.200619	9.833	8.853	8.583	−123.45	0.24
17274982–0506395	261.957593	−5.110977	11.076	10.281	10.081	−119.02	0.22
17275057–0504396	261.960714	−5.077668	9.395	8.384	8.089	−121.31	0.31
17275683–0504051	261.986826	−5.068087	10.676	9.788	9.546	−122.43	0.18
17275811–0501218	261.992155	−5.022726	9.949	9.006	8.718	−123.42	0.23
17280180–0507277	262.007524	−5.124366	11.130	10.329	10.111	−120.88	0.23
17280547–0502047	262.022809	−5.034661	9.596	8.572	8.309	−121.48	0.28
Hydra Probable Non-Members							
17255789–0458546	261.491242	−4.981845	10.464	9.482	9.187	+40.71	0.40
17260595–0513249	261.524819	−5.223611	11.025	10.013	9.688	−117.14	0.36
17261100–0514439	261.545871	−5.245550	10.534	9.692	9.454	+43.06	0.19
17263463–0508564	261.644297	−5.149007	11.352	10.435	10.205	+25.02	0.20
17263699–0523021	261.654149	−5.383922	10.810	9.944	9.770	+54.68	0.18
17263709–0447537	261.654575	−4.798261	10.191	9.280	8.983	+23.81	0.21
17263955–0513427	261.664802	−5.228553	10.838	9.740	9.415	+105.29	0.46
17264946–0450003	261.706092	−4.833436	10.443	9.480	9.122	+67.55	0.46
17265327–0511019	261.721975	−5.183884	11.215	10.308	10.027	+96.86	0.25
17265679–0458163	261.736648	−4.971201	9.519	8.452	8.057	−78.38	2.07
17265821–0513464	261.742548	−5.229565	10.581	9.530	9.200	+12.90	0.44
17265901–0437299	261.745876	−4.624999	9.940	8.858	8.526	−104.49	0.51
17270635–0511447	261.776467	−5.195766	10.789	9.773	9.464	−42.22	0.36
17270794–0438448	261.783086	−4.645779	10.144	9.045	8.733	−148.51	0.86
17271236–0446567	261.801531	−4.782440	11.168	10.345	10.110	+58.06	4.09
17271261–0511574	261.802555	−5.199298	11.590	10.517	10.223	−46.15	0.41
17272208–0527013	261.842034	−5.450384	10.329	9.384	9.091	−92.97	0.24
17273428–0526069	261.892859	−5.435271	11.066	10.314	10.061	−78.61	0.22
17274666–0512061	261.944417	−5.201704	9.704	8.747	8.414	+71.94	0.58
17280295–0509455	262.012312	−5.162657	11.224	10.481	10.269	+55.02	0.23
17280791–0456141	262.032985	−4.937277	10.554	9.549	9.254	+53.78	0.31
17280997–0500041	262.041543	−5.001159	11.065	10.149	9.971	+9.07	0.23
17281257–0506430	262.052380	−5.111953	9.487	8.632	8.322	+7.21	0.29
17281658–0437371	262.069099	−4.626997	10.298	9.425	9.170	+30.38	0.31

Table 2—Continued

Star Name (2MASS)	RA (J2000) (Degrees)	DEC (J2000) (Degrees)	J (mag.)	H (mag.)	K _S (mag.)	RV _{helio.} (km s ⁻¹)	RV Error (km s ⁻¹)
17282141–0527043	262.089211	−5.451209	10.406	9.454	9.141	−39.47	0.27
17284000–0506557	262.166707	−5.115496	10.237	9.298	8.977	−30.09	0.47
17284713–0517356	262.196415	−5.293239	10.638	9.702	9.457	−44.65	0.22
17284827–0443511	262.201140	−4.730881	11.212	10.344	10.088	+65.04	0.58
17285076–0511360	262.211504	−5.193343	10.125	9.228	8.996	+31.18	0.24
17291922–0447570	262.330122	−4.799176	10.964	10.170	9.940	+15.92	0.20
17292260–0516203	262.344189	−5.272316	11.015	10.101	9.836	−15.10	0.26
17292502–0455071	262.354280	−4.918642	10.532	9.708	9.481	+10.36	0.24

Table 3. NGC 6342 and NGC 6366 Stellar Atmosphere Parameters and Abundance Ratios

Star Name (2MASS)	T _{eff} (K)	log(g) (cgs)	[Fe/H] (dex)	$\xi_{\text{mic.}}$ (km s ⁻¹)	[O/Fe] (dex)	[Na/Fe] (dex)	[Mg/Fe] (dex)	[Si/Fe] (dex)	[Ca/Fe] (dex)	[Cr/Fe] (dex)	[Ni/Fe] (dex)	[La/Fe] (dex)
NGC 6342												
17205345–1957303	4600	2.20	−0.41	2.05	...	−0.16	...	+0.32	+0.15	...	−0.04	+0.28
17210009–1935354	4200	1.50	−0.59	1.70	+0.45	+0.17	...	+0.44	+0.00	−0.05
17210680–1935191	4850	2.75	−0.49	1.55	...	−0.08	...	+0.49	+0.22	...	−0.04	+0.31
17211185–1934551	4175	1.40	−0.65	2.20	+0.77	+0.02	+0.37	+0.41	+0.29	−0.13	+0.10	+0.12
NGC 6366												
17271061–0457415	4575	2.15	−0.66	2.00	+0.67	+0.46	+0.36	+0.35	+0.40	+0.16	+0.12	+0.33
17272071–0505087	4650	2.45	−0.47	1.90	+0.57	+0.03	+0.26	+0.22	+0.22	−0.21	+0.09	+0.29
17273010–0504197	4400	1.80	−0.47	1.60	+0.27	+0.27	+0.29	+0.21	+0.33	−0.04	...	+0.14
17273285–0500304	4375	1.75	−0.63	1.70	+0.60	−0.11	+0.30	+0.35	+0.17	...	+0.15	+0.00
17274128–0505308	4550	2.05	−0.60	1.65	+0.58	+0.21	+0.37	+0.23	+0.44	−0.03	+0.02	+0.17
17274221–0506173	4400	1.65	−0.67	2.15	+0.67	+0.25	+0.41	+0.18	+0.48	+0.17	+0.18	+0.19
17274279–0504077	4475	2.00	−0.42	1.70	+0.43	+0.18	+0.14	+0.35	+0.31	−0.13	+0.10	+0.19
17274541–0504089	4500	1.95	−0.62	1.80	+0.52	+0.27	+0.34	+0.26	+0.38	+0.09	+0.07	+0.26
17274724–0500362	4350	1.75	−0.47	1.90	+0.40	+0.12	+0.14	+0.44	+0.20	...	+0.05	+0.09
17274809–0507395	4525	2.10	−0.52	1.65	+0.32	+0.38	+0.34	+0.33	+0.37	+0.08	+0.01	+0.24
17274982–0506395	4475	1.60	−0.60	1.75	+0.60	−0.09	+0.27	+0.25	+0.19	−0.24	+0.15	+0.14
17275683–0504051	4400	1.75	−0.62	1.90	+0.59	+0.06	+0.34	+0.18	+0.31	−0.02	+0.09	+0.19
17280180–0507277	4550	2.15	−0.41	1.65	+0.36	+0.04	+0.23	+0.34	+0.16	...	+0.14	+0.13

Table 4. Line List and Adopted Reference Abundances

Species	Wavelength (Å)	E.P. (eV)	$\log(gf)^a$	$\log \epsilon(X)_{\odot}$ (dex)	$\log \epsilon(X)_{Arc.}$ (dex)	[X/Fe] or [Fe/H] _{Arc.} (dex)
[O I]	6300.30	0.00	-9.750	8.69	8.63	+0.44
Na I	6154.23	2.10	-1.560	6.33	5.89	+0.06
Na I	6160.75	2.10	-1.210	6.33	5.89	+0.06
Mg I	6318.71	5.10	-2.010	7.58	7.38	+0.30
Mg I	6319.24	5.10	-2.250	7.58	7.38	+0.30
Mg I	6319.49	5.10	-2.730	7.58	7.38	+0.30
Si I	6142.48	5.62	-1.575	7.55	7.38	+0.33
Si I	6145.02	5.62	-1.460	7.55	7.38	+0.33
Si I	6155.13	5.62	-0.774	7.55	7.38	+0.33
Si I	6155.69	5.62	-2.352	7.55	7.38	+0.33
Si I	6195.43	5.87	-1.560	7.55	7.38	+0.33
Si I	6237.32	5.61	-1.115	7.55	7.38	+0.33
Si I	6244.47	5.62	-1.303	7.55	7.38	+0.33
Ca I	6122.22	1.89	-0.466	6.36	6.07	+0.21
Ca I	6156.02	2.52	-2.637	6.36	6.07	+0.21
Ca I	6161.30	2.52	-1.246	6.36	6.07	+0.21
Ca I	6162.17	1.90	-0.210	6.36	6.07	+0.21
Ca I	6166.44	2.52	-1.262	6.36	6.07	+0.21
Ca I	6169.04	2.52	-0.837	6.36	6.07	+0.21
Ca I	6169.56	2.53	-0.628	6.36	6.07	+0.21
Cr I	6330.09	0.94	-3.000	5.67	5.09	-0.08
Fe I	6094.37	4.65	-1.700	7.52	7.02	-0.50
Fe I	6100.27	4.56	-2.116	7.52	7.02	-0.50
Fe I	6151.62	2.18	-3.379	7.52	7.02	-0.50
Fe I	6159.37	4.61	-1.950	7.52	7.02	-0.50
Fe I	6165.36	4.14	-1.584	7.52	7.02	-0.50
Fe I	6173.33	2.22	-2.930	7.52	7.02	-0.50
Fe I	6180.20	2.73	-2.629	7.52	7.02	-0.50
Fe I	6187.99	3.94	-1.690	7.52	7.02	-0.50
Fe I	6200.31	2.61	-2.437	7.52	7.02	-0.50

Table 4—Continued

Species	Wavelength (Å)	E.P. (eV)	$\log(gf)^a$	$\log \epsilon(X)_{\odot}$ (dex)	$\log \epsilon(X)_{Arc.}$ (dex)	[X/Fe] or [Fe/H] _{Arc.} (dex)
Fe I	6219.28	2.20	−2.563	7.52	7.02	−0.50
Fe I	6229.23	2.85	−2.885	7.52	7.02	−0.50
Fe I	6232.64	3.65	−1.263	7.52	7.02	−0.50
Fe I	6240.65	2.22	−3.353	7.52	7.02	−0.50
Fe I	6252.56	2.40	−1.847	7.52	7.02	−0.50
Fe I	6253.83	4.73	−1.500	7.52	7.02	−0.50
Fe I	6270.22	2.86	−2.649	7.52	7.02	−0.50
Fe I	6315.81	4.08	−1.720	7.52	7.02	−0.50
Fe I	6322.69	2.59	−2.446	7.52	7.02	−0.50
Fe I	6330.85	4.73	−1.230	7.52	7.02	−0.50
Fe I	6335.33	2.20	−2.387	7.52	7.02	−0.50
Fe I	6336.82	3.69	−0.866	7.52	7.02	−0.50
Ni I	6128.96	1.68	−3.400	6.25	5.81	+0.06
Ni I	6130.13	4.27	−1.040	6.25	5.81	+0.06
Ni I	6175.36	4.09	−0.619	6.25	5.81	+0.06
Ni I	6176.81	4.09	−0.270	6.25	5.81	+0.06
Ni I	6177.24	1.83	−3.550	6.25	5.81	+0.06
Ni I	6186.71	4.11	−0.890	6.25	5.81	+0.06
Ni I	6191.17	1.68	−2.233	6.25	5.81	+0.06
Ni I	6223.98	4.11	−0.960	6.25	5.81	+0.06
Ni I	6322.16	4.15	−1.190	6.25	5.81	+0.06
La II	6262.29	0.40	hfs	1.13	0.57	−0.06

^aThe “hfs” designation indicates the abundance was calculated by taking hyperfine structure into account. See text for details.

Table 5. NGC 6342 and NGC 6366 Abundance Ratio Uncertainties

Star Name (2MASS)	$\Delta[\text{Fe}/\text{H}]$ (dex)	$\Delta[\text{O}/\text{Fe}]$ (dex)	$\Delta[\text{Na}/\text{Fe}]$ (dex)	$\Delta[\text{Mg}/\text{Fe}]$ (dex)	$\Delta[\text{Si}/\text{Fe}]$ (dex)	$\Delta[\text{Ca}/\text{Fe}]$ (dex)	$\Delta[\text{Cr}/\text{Fe}]$ (dex)	$\Delta[\text{Ni}/\text{Fe}]$ (dex)	$[\Delta\text{La}/\text{Fe}]$ (dex)
NGC 6342									
17205345–1957303	0.05	...	0.09	...	0.08	0.12	...	0.09	0.09
17210009–1935354	0.06	0.10	0.10	...	0.10	0.13	0.10
17210680–1935191	0.06	...	0.09	...	0.09	0.13	...	0.09	0.09
17211185–1934551	0.04	0.08	0.09	0.05	0.07	0.12	0.13	0.10	0.08
NGC 6366									
17271061–0457415	0.05	0.09	0.07	0.08	0.12	0.09	0.11	0.07	0.09
17272071–0505087	0.05	0.09	0.06	0.07	0.08	0.09	0.11	0.07	0.09
17273010–0504197	0.06	0.10	0.08	0.06	0.09	0.11	0.13	...	0.09
17273285–0500304	0.06	0.10	0.07	0.06	0.09	0.11	...	0.11	0.09
17274128–0505308	0.06	0.10	0.07	0.08	0.08	0.09	0.12	0.11	0.09
17274221–0506173	0.05	0.09	0.07	0.08	0.08	0.10	0.12	0.08	0.09
17274279–0504077	0.07	0.10	0.08	0.07	0.11	0.10	0.13	0.09	0.10
17274541–0504089	0.05	0.09	0.07	0.05	0.07	0.09	0.12	0.08	0.09
17274724–0500362	0.06	0.10	0.08	0.08	0.09	0.11	...	0.09	0.09
17274809–0507395	0.06	0.09	0.10	0.06	0.11	0.10	0.12	0.09	0.09
17274982–0506395	0.07	0.10	0.10	0.07	0.08	0.10	0.12	0.10	0.10
17275683–0504051	0.05	0.09	0.09	0.11	0.09	0.09	0.12	0.07	0.09
17280180–0507277	0.06	0.10	0.08	0.09	0.07	0.10	...	0.09	0.10

Table 6. Composition Comparison: $-0.7 \leq [\text{Fe}/\text{H}] \leq -0.4$

Average [X/Fe]	NGC 6342	NGC 6366	Bulge Clusters ^a	Bulge Clusters ^b	Bulge Field
$\langle [\text{O}/\text{Fe}] \rangle$	+0.61	+0.51	+0.48	+0.16	+0.47
$\langle [\text{Na}/\text{Fe}] \rangle$	-0.01	+0.16	+0.17	+0.36	-0.01
$\langle [\text{Mg}/\text{Fe}] \rangle$	+0.37	+0.29	+0.39	+0.34	+0.31
$\langle [\text{Si}/\text{Fe}] \rangle$	+0.42	+0.28	+0.29	+0.31	+0.29
$\langle [\text{Ca}/\text{Fe}] \rangle$	+0.22	+0.30	+0.31	+0.22	+0.26
$\langle [\text{Cr}/\text{Fe}] \rangle$	-0.13	-0.02	-0.07	-0.08	+0.01
$\langle [\text{Ni}/\text{Fe}] \rangle$	+0.01	+0.10	-0.04	+0.02	+0.06
$\langle [\text{La}/\text{Fe}] \rangle$	+0.17	+0.18	...	+0.36	-0.20
Abundance Dispersions					
$\sigma[\text{O}/\text{Fe}]$	0.23	0.13	0.07	0.32	0.15
$\sigma[\text{Na}/\text{Fe}]$	0.14	0.17	0.15	0.25	0.12
$\sigma[\text{Mg}/\text{Fe}]$...	0.08	0.07	0.11	0.09
$\sigma[\text{Si}/\text{Fe}]$	0.07	0.08	0.09	0.12	0.11
$\sigma[\text{Ca}/\text{Fe}]$	0.07	0.11	0.10	0.16	0.11
$\sigma[\text{Cr}/\text{Fe}]$...	0.14	0.03	0.18	0.10
$\sigma[\text{Ni}/\text{Fe}]$	0.07	0.05	0.05	0.09	0.05
$\sigma[\text{La}/\text{Fe}]$	0.17	0.09	...	0.09	0.08

^aNGC 6388 and NGC 6441 are omitted.

^bAll bulge globular clusters with $-0.7 \leq [\text{Fe}/\text{H}] \leq -0.4$ are included.

Table 7. Literature References

Stellar Population	Reference
HP-1	Barbuy et al. (2006)
NGC 6342	Origlia et al. (2005a)
NGC 6352	Feltzing et al. (2009)
NGC 6388	Carretta et al. (2007)
NGC 6388	Carretta et al. (2009a)
NGC 6388	Worley & Cottrell (2010)
NGC 6440	Origlia et al. (2008)
NGC 6441	Gratton et al. (2006)
NGC 6441	Gratton et al. (2007)
NGC 6441	Origlia et al. (2008)
NGC 6528	Carretta et al. (2001)
NGC 6528	Origlia et al. (2005a)
NGC 6539	Origlia et al. (2005b)
NGC 6553	Cohen et al. (1999)
NGC 6553	Meléndez et al. (2003)
NGC 6553	Alves-Brito et al. (2006)
NGC 6553	Johnson et al. (2014)
NGC 6569	Valenti et al. (2011)
NGC 6624	Valenti et al. (2011)
Terzan 5	Origlia et al. (2011)
Terzan 5	Origlia et al. (2013)
UKS 1	Origlia et al. (2005b)
Galactic Bulge	Alves-Brito et al. (2010)
Galactic Bulge	Gonzalez et al. (2011)
Galactic Bulge	Hill et al. (2011)
Galactic Bulge	Johnson et al. (2011)
Galactic Bulge	Johnson et al. (2012)
Galactic Bulge	Bensby et al. (2013)
Galactic Bulge	Johnson et al. (2013)
Galactic Bulge	Johnson et al. (2014)